Monthly Notices of the ROYAL ASTRONOMICAL SOCIETY

MNRAS **514,** 2407–2424 (2022)
Advance Access publication 2022 June 2

https://doi.org/10.1093/mnras/stac1367

The extinction law in the inner 3 × 3 deg^2 of the Milky Way and the red clump absolute magnitude in the inner bar-bulge

Jason L. Sanders [1]★ Leigh Smith,[2] Carlos González-Fernández [2], Philip Lucas [3] and Dante Minniti[4,5]

[1]*Department of Physics and Astronomy, University College London, London WC1E 6BT, UK*
[2]*Institute of Astronomy, University of Cambridge, Madingley Rise, Cambridge CB3 0HA, UK*
[3]*Centre for Astrophysics, University of Hertfordshire, College Lane, Hatfield AL10 9AB, UK*
[4]*Departamento de Ciencias Físicas, Facultad de Ciencias Exactas, Universidad Andrés Bello, Fernández Concha 700, Las Condes, Santiago, Chile*
[5]*Vatican Observatory, Vatican City State I-V-00120, Italy*

Accepted 2022 May 10. Received 2022 May 10; in original form 2022 April 7

ABSTRACT

The extinction law from 0.9 to 8 microns in the inner $3 \times 3\,\mathrm{deg}^2$ of the Milky Way is measured using data from VISTA Variables in the Via Lactea, GLIMPSE, and *WISE*. Absolute extinction ratios are found by requiring that the observed red clump density peaks at the GRAVITY collaboration distance to the Galactic centre. When combined with selective extinction ratios measured from the bulge giant colour–colour diagrams, we find an extinction law of $A_Z : A_Y : A_J : A_H : A_{K_s} : A_{W1} : A_{[3.6]} : A_{[4.5]} : A_{W2} : A_{[5.8]} : A_{[8.0]} = 7.19(0.30) : 5.11(0.20) : 3.23(0.11) : 1.77(0.04) : 1 : 0.54(0.02) : 0.46(0.03) : 0.34(0.03) : 0.32(0.03) : 0.24(0.04) : 0.28(0.03)$ valid for low extinctions where non-linearities are unimportant. These results imply an extinction law from the Rayleigh Jeans colour excess method of $A_{K_s} = 0.677(H - [4.5] - 0.188)$. We find little evidence for significant selective extinction ratio variation over the inspected region (around 5 per cent). Assuming the absolute extinction ratios do not vary across the inspected region gives an independent measurement of the absolute K_s magnitude of the red clump at the Galactic Centre of (-1.61 ± 0.07) mag. This is very similar to the value measured for solar neighbourhood red clump stars giving confidence in the use of red clump stars as standard candles across the Galaxy. As part of our analysis, we inspect the completeness of PSF photometry from the VVV survey using artificial star tests, finding 90 per cent completeness at $K_s \approx 16\,(17)$ in high (low) density regions and good agreement with the number counts with respect to the GALACTICNUCLEUS and DECAPS catalogues over small regions of the survey.

Key words: stars: distances – dust, extinction – Galaxy: bulge.

1 INTRODUCTION

The inner parts of the Milky Way contain important information on the formation and history of our Galaxy and provide a detailed window into the nuclear properties of a Milky-Way-like galaxy. Near- and mid-infrared surveys such as 2MASS, VVV, UKIDSS, and GLIMPSE have allowed studies to probe through the interstellar dust to infer the morphological properties of this region. On scales of $\ell \lesssim 10$ deg the Galactic bar/bulge is the dominant structure (e.g. Blitz & Spergel 1991; Stanek et al. 1994, 1997; Babusiaux & Gilmore 2005; Rattenbury et al. 2007; McWilliam & Zoccali 2010; Wegg & Gerhard 2013; Simion et al. 2017; Sanders et al. 2019), and at larger radii, the bar/bulge extends into the long thin bar (Wegg, Gerhard & Portail 2015). In the very central regions around the suspected dynamical centre of the Galaxy, Sgr A∗, there is a nuclear stellar cluster (NSC; Schödel et al. 2014), and between these two structures sits the nuclear stellar disc (Launhardt, Zylka & Mezger 2002; Nishiyama et al. 2013; Sormani et al. 2022). The nuclear stellar disc has an extent of $\ell \sim 1.5$ deg and is associated with the central x2 orbits that form in a barred potential. Compared to the bar/bulge and the NSC, the nuclear stellar disc has been little studied. Nogueras-Lara et al. (2020a) recently argued that the nuclear stellar disc is composed almost entirely of stars older than 8 Gyr although there is evidence of a more recent starburst. This points towards a picture where the bulk of the stars in the nuclear stellar disc formed at bar formation when gas rapidly funnelled to the centre, but since then the gas supply and hence star formation has been more gentle until possibly a recent episode.

Many of the highlighted studies on the structure of the inner Galaxy rely on the standard candle nature of red clump stars (Girardi 2016). Red clump stars are metal-rich core helium burning and, particularly in the K_s band, display a small scatter in absolute magnitude (Alves 2000; Hawkins et al. 2017; Hall et al. 2019; Chan & Bovy 2020). For this reason, they have found use beyond the Milky Way, for example in the Magellanic Clouds (Alves et al. 2002; Pietrzyński & Gieren 2002) and M31 (Stanek & Garnavich 1998). Variations in the red clump's absolute magnitude with both age and metallicity are expected (Girardi & Salaris 2001) and observed (Chen et al. 2017; Chan & Bovy 2020; Huang et al. 2020). This means for highly accurate density mapping of the central Galaxy we require knowledge of its age and metallicity structure. Alternatively, with a known density structure we could use the red clump to infer the age and metallicity of the inner Galaxy (Nogueras-Lara et al. 2020a).

★ E-mail: jason.sanders@ucl.ac.uk

These approaches are complicated by extinction, which is particularly severe in the inner regions of the Milky Way ($A_V \approx 40$ towards the Galactic Centre; Nishiyama et al. 2008; Schödel et al. 2010). In the absence of additional information, there are degeneracies between the absolute magnitude of the red clump, the distances to the stars, and the shape of the extinction curve. For structural studies of the inner Galaxy, the extinction curve shape is a key parameter. Matsunaga et al. (2018) gives a review of measurements of the extinction law in the near- and mid-infrared. In recent years, studies have settled on a steep extinction law in the near-infrared with power-law index α ($A_x \propto \lambda_x^{-\alpha}$) around $\alpha = 2 - 2.2$ (Nishiyama et al. 2009; Stead & Hoare 2009; Schödel et al. 2010; Fritz et al. 2011; Alonso-García et al. 2017; Nogueras-Lara et al. 2019a; Maíz Apellániz et al. 2020; Stelter & Eikenberry 2021). The universality of the extinction law is less certain with variations reported as a function of location in the Galaxy (Zasowski et al. 2009) and total extinction/density of intervening clouds (Chapman et al. 2009), although Wang & Jiang (2014) argue for a universality of the near-infrared extinction law.

Until the measurements of the distance to Sgr A∗ from Gravity Collaboration (2019, 2021), a reference distance to the bar/bulge red clump stars was not known. Instead several studies have inferred the distance to the Galactic Centre using assumptions for the red clump absolute magnitude based on observations of solar neighbourhood stars (Paczyński & Stanek 1998; Nishiyama et al. 2006). The degeneracies between absolute magnitude, distance, and extinction make these studies challenging. However, with the distance to the Galactic Centre now more confidently measured, we are in a position to break some of this degeneracy under the assumption that Sgr A∗ is the dynamical centre of the Galaxy.

In this paper, we derive the extinction curve of the inner $3 \times 3\,\mathrm{deg}^2$ of the Galaxy from 0.9 to 8 microns. We use a novel method that pins the unextincted magnitude of the red clump based on the known distance to the Galactic Centre from Gravity Collaboration (2021). In this way, we are able to not only infer the extinction law but also the absolute magnitude of red clump stars at the Galactic centre. We combine this method with more traditional colour excess methods to derive the full extinction curve. We outline and apply the colour excess method in Section 2, and the calibration of the absolute extinction curve and a discussion of the absolute red clump magnitude are presented in Section 3. From this extinction curve, we derive 2D extinction maps (neglecting distance dependence) using both the known colours of red clump stars (Gonzalez et al. 2011, 2012; Surot et al. 2020) and the ($H - [4.5]$) colour of all stars (Majewski, Zasowski & Nidever 2011) as presented in Appendix B1 and B2. We further present a brief discussion of the completeness properties of a point-spread-function photometric reduction of VVV in Appendix C. We close with our conclusions in Section 4.

2 SELECTIVE EXTINCTION RATIOS FROM 1 TO 8 MICRONS

In this section, we consider measuring the selective extinction ratios for the inner Galaxy. It is much easier to estimate selective extinction ratios than any absolute to selective extinction ratio as we only require observed colours of known stellar types, not knowledge of the distances to the sources. However, with a set of selective ratios and a single absolute to selective ratio, we can compute all absolute extinction ratios.

An extinction law $A(\lambda)$ describes the reduction in magnitudes at a given wavelength λ. The extinction in a photometric band x with (photon-counting) transmission $T_x(\lambda)$ for a star with flux $F_\lambda(\lambda)$ is

$$A_x = -2.5 \log_{10} \left(\int \mathrm{d}\lambda\, \lambda T_x F_\lambda 10^{-0.4A(\lambda)} \Big/ \int \mathrm{d}\lambda\, \lambda T_x F_\lambda \right), \quad (1)$$

from which we can define the selective extinction for colour $x - y$ as $E(x - y) \equiv A_x - A_y$. For low extinction, the integral is approximately linear in $A(\lambda)$ and for narrow bands A_x is approximately independent of $F_\lambda(\lambda)$. In these limits, the extinction coefficients normalized with respect to the extinction at some reference wavelength, $A_x/A(\lambda_{\mathrm{ref}})$, are independent of total extinction and stellar type. In this case, a universal extinction law can be applied to all stars and we characterize the extinction law by constant absolute ratios e.g. A_x/A_{K_s} from which constant selective extinctions ratios can be computed e.g. $E(x - K_s)/E(y - K_s) = (A_x/A_{K_s} - 1)/(A_y/A_{K_s} - 1)$.

Assuming non-linear effects are minimal, for some colour c, the extinction law is given by

$$A_{K_s} = R_c E(c), \quad (2)$$

for a constant R_c. Our aim is to measure $E(c)/E(H - K_s) = R_{H-K_s}/R_c$. We consider red giant stars which are known to follow trends in colour–magnitude space related to correlations between luminosity and temperature. As our samples are located predominantly in the Galactic bulge, these correlations are imprinted on the dereddened colour–magnitude diagrams. It is therefore important to consider this 'intrinsic' correlation in addition to correlations induced by extinction. Assuming the absolute K_s magnitude is a simple linear function of colour for giant stars at a single distance, we have

$$K_s' = (c' - c_0)/k_c + K_{s0,c}, \quad (3)$$

where primed quantities are dereddened and c_0 and $K_{s0,\,c}$ are arbitrary constants. We measure k_c from a set of PARSEC isochrones with [M/H] = 0 and log (age/Gyr) > 9.5 (Bressan et al. 2012; Chen et al. 2014, 2015; Tang et al. 2014; Marigo et al. 2017). Using these relations we can relate the observed $(H - K_s)$ colour to any other colour, c, as

$$(H - K_s) - k_{H-K_s} K_s = \frac{R_c}{R_{H-K_s}} \frac{1 - k_{H-K_s} R_{H-K_s}}{\times\ 1 - k_c R_c (c - k_c K_s) + \mathrm{const.}}, \quad (4)$$

so the gradient g_c of a linear fit of $c - k_c K_s$ against $(H - K_s) - k_{H-K_s} K_s$ will recover the extinction ratio $E(c)/E(H - K_s)$ as

$$\frac{E(c)}{E(H - K_s)} = g_c + R_{H-K_s}(k_c - g_c k_{H-K_s}). \quad (5)$$

Note that this method requires knowledge of the absolute extinction ratio R_{H-K_s} to measure $E(c)/E(H - K_s)$. However, the dependence is weak as k_c for near- and mid-infrared bands is typically small so we adopt a standard value from Fritz et al. (2011) of $R_{H-K_s} = 1.328$ (using $R_{H-K_s} = 1.104$ from Alonso-García et al. (2017) results in changes to $E(c)/E(H - K_s)$ of less than 0.5 per cent). We note that it is possible to use a version of equation (4) dependent on $E(H - K_s)$ measured from red clump stars. However, we find in general this method is less accurate than using colour–colour relations, partly because of the underestimate of $E(H - K_s)_{\mathrm{RC}}$ for large extinction (see Appendix B1).

To fit equation (4) to data we employ a total least-squares procedure (Hogg, Bovy & Lang 2010). For a data vector $\mathbf{Z}_i = (c_i - k_c K_{si}, (H - K_s)_i - k_{H-K_s} K_{si})$ and corresponding covariance matrix $\mathbf{\Sigma}_i$ we seek the straight line that maximizes the log-likelihood

$$\ln \mathcal{L} = -\tfrac{1}{2} \sum_i \ln(\boldsymbol{v}^{\mathrm{T}} \Sigma_i \boldsymbol{v} + \sigma^2) + \frac{(\boldsymbol{v}^{\mathrm{T}} \mathbf{Z}_i - b_\perp)^2}{\boldsymbol{v}^{\mathrm{T}} \Sigma_i \boldsymbol{v} + \sigma^2}, \quad (6)$$

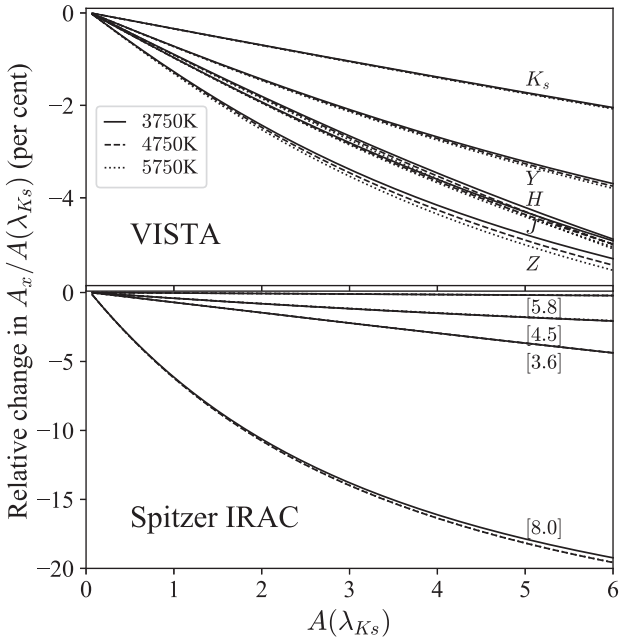

Figure 1. Non-linearity of the extinction law: we display curves of the relative percentage change in the extinction in band x, A_x (evaluated using equation 1), normalized by the extinction evaluated at $\lambda_{K_s} = 2.149$ μm. We adopt the extinction curve from Fritz et al. (2011) and use three different giant stellar spectra.

where $\boldsymbol{v} = (-\sin\theta, \cos\theta)$, θ is the angle of the line with respect to the 'x' coordinate, $b_\perp = b\cos\theta$ with b the 'y' intercept of the line. We adopt flat priors in θ and $b_\perp$. We add in an additional variance σ^2 to account for the width of the giant branch. Additionally, we choose to include an outlier component which a different straight line with a broader variance $\sigma^2_{\rm out}$. The weight of the outlier component is $f_{\rm out}$ which we limit to be less than 0.4. We sum the likelihood of this term with the model likelihood (times $(1-f_{\rm out})$). The maximum likelihood is found through using BFGS minimization with the Jacobian computed using AUTOGRAD.[1] The uncertainty in the output gradient is estimated using the inverse of the Hessian matrix (also computed using AUTOGRAD).

2.1 Non-linearity of extinction coefficients

For high extinction regions, the non-linearity in the extinction calculation of equation (1) can become important (e.g. Stead & Hoare 2009; Wang & Chen 2019; Maíz Apellániz et al. 2020). We assess the impact of the non-linearity by computing equation (1) for the VISTA and *Spitzer* passbands (downloaded from the SVO filter service; Rodrigo, Solano & Bayo 2012; Rodrigo & Solano 2020). We use three different stellar spectra from Castelli & Kurucz (2003) with $T_{\rm eff} = (3750, 4750, 5750)$ K, $\log g = (0.5, 2.5, 3.5)$ and solar metallicity. We use the extinction law from Fritz et al. (2011). In Fig. 1 we display the percentage relative change in A_x normalized by the extinction at $\lambda_{K_s} = 2.149$ μm, A_{K_s}, against A_{K_s}. Most bands have relative changes of a few per cent over the range of considered extinctions ($A(\lambda_{K_s}) < 6$, typically extinctions in the inner Galaxy are $A(\lambda_{K_s} < 3)$ and in general, the bluer VISTA bands have larger changes than the *Spitzer* bands, except for [8.0] for which there is a large evolution of $A_{[8.0]}/A(\lambda_{K_s})$ of approximately 5 per cent per magnitude of $A(\lambda_{K_s})$. This arises due to the 9.7 μm silicate feature. From these calculations, we store the variation of $\mathrm{NL}_c(E(H-K_s)) = E(c)/E(H-K_s) - E(c)/E(H-K_s)|_{A_x\to 0}$ as a function of $E(H-K_s)$ for the $T_{\rm eff} = 4750$ K, $\log g = 2.5$ model to simply correct the colours of stars for typical non-linear effects as $c \leftarrow c - E(H-K_s)\mathrm{NL}_c(E(H-K_s))$ using $E(H-K_s) \approx (H-K_s - 0.1)$.

2.2 Data

Our primary source of data is the preliminary VIRAC2 catalogue (Smith et al. 2018; Smith et al., in preparation). VIRAC2 is an updated version of the VVV InfraRed Astrometric Catalogue presented by Smith et al. (2018). VVV is a near-infrared multi-epoch photometric survey of the Galactic bulge and southern Galactic disc performed using the VIRCAM detector (Dalton et al. 2006) with pixel resolution of 0.339 arcsec on the 4 m VISTA telescope at the Cerro Paranal Observatory (with typical seeing of ~ 0.7 arcsec). The original VVV survey ran from 2010 to 2015 but was granted a five-year extension (VVVX) from 2016. The primary multi-epoch observations consist of ~ 200 2×4 s K_s exposures with a typical depth of $K_s \sim 17$ in the region we consider (each pointing consists of two exposures 'jittered' by small offsets, hence the '$2\times$'). The K_s photometry is complemented by more sparsely sampled Z, Y, J, and H photometry (approximately 4, 4, 20–40, and 10–20 exposures of 2×10, 2×10, 4×6 (4×10 for VVVX) and 2×4 (2×6 for VVVX) seconds, respectively, see Saito et al. 2012 for details). There are no Z and Y observations as part of VVVX. Saturation effects in all bands occur around 11.5 to 13.0 mag (see fig. 12 of González-Fernández et al. 2018, for results with 5s exposures) and the typical depth is (20.5, 20, 19.5, 18.5, 18) mag in (Z, Y, J, H, K_s) (slightly deeper for the longer VVVX J and H exposures) although in the central bulge fields the depth is confusion-limited (see figs 3, 4, and 5 of Saito et al. 2012).

VIRAC2 consists of a complete re-reduction of the VVV and VVVX *ZYJHK*$_s$ images in the original VVV Galactic bulge and southern disc footprint utilizing point-spread-function photometry, employing a recalibration of the photometric zeropoints with respect to 2MASS (to address the issues highlighted by Hajdu et al. 2020) and combining multiple detections into astrometric solutions calibrated with respect to *Gaia*. Furthermore, as VVV begins to saturate around $K_s = 11.5$, we complement the VVV data set with brighter stars from 2MASS by finding any star in 2MASS without a counterpart in VIRAC2 within 1 arcsec and with $K_s > 11$. We put the 2MASS measurements on the VISTA system using the transformations from González-Fernández et al. (2018) and correct for small median photometric shifts in overlapping 2MASS and VIRAC2 measurements. We perform our procedure described in the previous section on all stars in VIRAC2 (combined with 2MASS) with $|\ell| < 1.5$ deg, $|b| < 1.5$ deg and $K_s < 13.5 - 1.33(H-K_s-0.09)$ (a cut approximately parallel to the extinction vector), five-parameter astrometric solutions, non-duplicates and without a neighbour in the data set within 1 arcsec. When using VIRAC2 *ZYJHK*$_s$ photometry we limit to magnitude uncertainties < 0.06 mag and magnitudes brighter than 19. For 2MASS sources, we limit to uncertainties < 0.2 mag. We cross-match the sources to sources in GLIMPSE (using sources with `sqf_*=0` from Churchwell et al. 2009 or `f*=1` from Ramírez et al. 2008) and unWISE (Schlafly, Meisner & Green 2019, using sources with no flags) with a cross-match radius of 0.4 arcsec and 1 arcsec respectively (again limiting to stars with magnitude uncertainties < 0.2 mag). Our other cuts, in particular the VIRAC2 nearest neighbour cut, are such that essentially all the VIRAC2

[1] https://github.com/HIPS/autograd

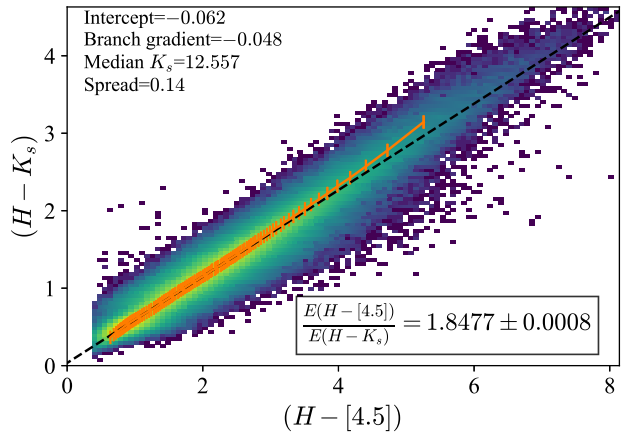

Figure 2. Example of a colour–colour giant branch fit to find the selective extinction ratio for $E(H-[4.5])/E(H-K_s)$. The background histogram shows the full data distribution coloured using a log-scale. The orange is the binned median, whilst the black-dashed shows a linear fit using a total least-squares approach. The 'intercept' gives the x-intercept of the fit, 'branch gradient' is the slope of the giant branch in $(H-[4.5]$ versus K_s, and 'spread' is the standard deviation about the linear fit.

sources we use are assigned to unique (or no) *WISE*/GLIMPSE sources. One source is cross-matched to two unWISE sources. When using *WISE*, we also ensure there is a corresponding GLIMPSE detection. To eliminate foreground contaminants, we further remove stars with $(H-K_s)+2\sqrt{\sigma_H^2+\sigma_{K_s}^2} < 0.09 + E(H-K_s)_{\rm RC} - 2\sigma_{E(H-K_s)_{\rm RC}}$ or $(J-K_s)+2\sqrt{\sigma_J^2+\sigma_{K_s}^2} < 0.62 + E(J-K_s)_{\rm RC} - 2\sigma_{E(J-K_s)_{\rm RC}}$ using extinction estimates from the red clump method (Appendix B1). Note this procedure is valid even when $E(J-K_s)_{\rm RC}$ and $E(H-K_s)_{\rm RC}$ are biased low due to the absence of the red clump in high extinction regions. We further remove likely AGB or YSOs by removing stars with $([5.8]-[8.0])/\sqrt{\sigma_{[5.8]}^2+\sigma_{[8.0]}^2} > 5$. The extinction coefficient in [5.8] is smaller than [8.0] (see Wang & Chen 2019) so this does not remove highly extincted giant stars. Cross-matching this sample to GALACTICNUCLEUS (Nogueras-Lara et al. 2019b, with a 0.1 arcsec cross-match radius) and restricting to stars with $K_s < 14$ and VIRAC uncertainties < 0.02 mag gives zero-point offsets (GALACTICNUCLEUS - VIRAC) of $(J, H, K_s) = (-0.027, 0.008, 0.026)$.

For $x = \{Z, Y, J, [3.6], [4.5], [5.8], [8.0], W1, W2\}$ with $c = (x-H)$, we find the maximum-likelihood solution for the straight line fit as described earlier. The result of applying our procedure with $x = [4.5]$ is shown in Fig. 2 where we measure $E(H-[4.5])/E(H-K_s) = 1.8477 \pm 0.0008$ and $k_{[4.5]-H} = -0.021$. We present the results of our fitting procedure in Table 1. Note that the uncertainties are statistical and probably unrealistically small as they do not reflect systematic uncertainty from the simplicity of the employed model. We compare to the ratios to reported by Fritz et al. (2011, using hydrogen line absorption towards the Galactic Centre), Alonso-García et al. (2017, using the colour–magnitude slope of the bulge red clump stars), Nishiyama et al. (2009, using the colour–magnitude slope of giant stars in the bulge) and Wang & Chen (2019, using red clump stars from APOGEE distributed across the sky). It should be noted that as different studies use different instruments the infrared bands are not identical so some variation is to be expected. Using the $T_{\rm eff} = 4750$ K, $\log g = 2.5$ spectrum from Castelli & Kurucz (2003), we find $(A_{J_{\rm HAWK-I}}, A_{J_{\rm SIRIUS}}, A_{J_{\rm 2MASS}}) = (0.994, 1.012, 1.028)A_{J_{\rm VISTA}}$, $(A_{H_{\rm HAWK-I}}, A_{H_{\rm SIRIUS}}, A_{H_{\rm 2MASS}}) = (1.037, 1.021, 0.995)A_{H_{\rm VISTA}}$ and $(A_{K_{s,\rm HAWK-I}}, A_{K_{s,\rm SIRIUS}}, A_{K_{s,\rm 2MASS}}) = (1.012, 1.011, 0.991)A_{K_{s,\rm VISTA}}$.

2.3 Spatial variation

With the average selective extinction ratios over the inner 3×3 deg^2 computed, we now turn to the spatial variation of the selective extinction ratio. We repeat the above calculation for a series of on-sky bins. Starting with the whole considered region, we iteratively split the on-sky bins into four sub-bins until further splits would cause one sub-bin to have fewer than 500 stars or a total of four splits have already been performed (or two splits when considering *Spitzer*/GLIMPSE data). We adopt a stricter cut on *Spitzer*/GLIMPSE photometry uncertainties requiring magnitude errors smaller than 0.05 mag.

We display the results in Fig. 3 and in Table 1 we report the mean and standard deviation of the selective extinction ratios across the on-sky bins. In all bands, we find less than 5 per cent variation in $E(i-K_s)/E(H-K_s)$ across the region analysed, which translates into a few per cent variation in A_i/A_{K_s} for the bluer bands (Z, Y, J) and a few tens of per cent for the redder bands (e.g. [8.0]). Some part of the variation appears as noise, but there are also some clear systematic variations. For instance, there is a feature of the presented maps around $(\ell, b) = (1, 0)$ seen particularly in J and Y, but also seen in the *Spitzer* bands as a general underestimate. This feature also coincides with a problematic region for the 2D extinction maps (see Appendix B2 and Fig. B2) where it appears there is a significant population of young stars in this region which bias low the extinction to the red clump stars. This suggests along these lines-of-sight there is significant extinction variation. Foreground clouds could give rise to variation in the selective extinction ratios (e.g. Chapman et al. 2009). However, the variation we see could also be attributed to the contaminating young star population. Nishiyama et al. (2009), Alonso-García et al. (2017), and Nogueras-Lara et al. (2019a) all investigated the variation of the extinction law across the Galactic central regions. Alonso-García et al. (2017) tabulated the variation in the extinction law for four quadrants in the region $|l| \lesssim 2.7$ deg and $|b| \lesssim 1.55$ deg finding variation of order ~ 10 per cent for $E(i-H)/E(H-K_s)$ for $i \in \{Z, Y, J\}$ and in general higher values for the southern quadrants compared to northern. Nishiyama et al. (2009) found a similar 10 per cent variation in $E(J-H)/E(H-K_s)$ across the region $|l| \lesssim 3$ deg and $|b| \lesssim 1$ deg but instead with higher values observed in the northern quadrants (although as Alonso-García et al. 2017 report, the trend of lower $A_{K_s}/E(J-K_s)$ in the northern quadrants was found in both studies). Nogueras-Lara et al. (2019a) inspected the variation across the nuclear stellar disc ($|l| \lesssim 0.3$ deg and $|b| \lesssim 0.1$ deg) finding no significant variation in the slope of the extinction law. In conclusion, we find that the variation in the selective extinction law across the inner 3×3 deg^2 is small.

3 ABSOLUTE EXTINCTION RATIOS AND THE MAGNITUDE OF THE RED CLUMP

To convert the selective extinction ratios, $E(c)/E(H-K_s)$, of the previous section to absolute extinction ratios, A_x/A_{K_s}, we must adopt a reference absolute extinction ratio value of R_{H-K_s}. This can be measured using the slope of the red clump in colour–magnitude space (Alonso-García et al. 2017) or from the absorption of hydrogen lines as in the work of Fritz et al. (2011). Here we employ a method for estimating the absolute extinction ratios using the apparent K_s magnitude of the red clump. In the absence of other information, there is a complete degeneracy between extinction, distance, and absolute magnitude. Here we break the degeneracy by assuming a fixed absolute magnitude of the red clump and that the peak of the density distribution of red clump stars occurs at the Galactic centre distance from Gravity Collaboration (2021). Further, we shall see that using

Table 1. Colour excess ratio $E(x-H)/E(H-K_s)$ (left for the full region, right split into subpixels with the uncertainty showing the standard deviation) with the corresponding measurements from Fritz et al. (2011), Alonso-García et al. (2017), Nishiyama et al. (2009), Nogueras-Lara et al. (2019a) and Wang & Chen (2019). Wang & Chen (2019) use the *Spitzer* ratios from Chen et al. (2018). Note that Nishiyama et al. (2009) report coefficients for the SIRIUS bands, Wang & Chen (2019) for the 2MASS bands and Nogueras-Lara et al. (2019a) for the HAWK-I bands (see the end of Section 2.2 for approximate conversions).

$x-H$	$E(x-H)/E(H-K_s)$		Fritz et al. (2011)	Alonso-García et al. (2017)	Nishiyama et al. (2009)	Nogueras-Lara et al. (2019a)	Wang & Chen (2019)
Z	$+7.0010 \pm 0.0018$	$+7.07 \pm 0.25$	–	$+6.66 \pm 0.23$	–	–	–
Y	$+4.3119 \pm 0.0007$	$+4.38 \pm 0.18$	$+3.84 \pm 0.43$	$+3.98 \pm 0.13$	–	–	–
J	$+1.8788 \pm 0.0001$	$+1.98 \pm 0.08$	$+1.76 \pm 0.20$	$+1.61 \pm 0.05$	$+1.76 \pm 0.06$	$+2.09 \pm 0.05$	$+2.11 \pm 0.31$
[3.6]	-1.7034 ± 0.0008	-1.70 ± 0.04	-1.60 ± 0.30	–	-1.68 ± 0.11	–	-1.77 ± 0.47
[4.5]	-1.8477 ± 0.0008	-1.82 ± 0.07	-1.80 ± 0.33	–	-1.83 ± 0.12	–	-1.98 ± 0.51
[5.8]	-1.9861 ± 0.0006	-1.97 ± 0.06	-1.88 ± 0.34	–	-1.88 ± 0.12	–	-2.11 ± 0.53
[8.0]	-1.9264 ± 0.0007	-1.87 ± 0.08	-1.82 ± 0.35	–	-1.78 ± 0.11	–	-2.00 ± 0.51
$W1$	-1.5892 ± 0.0044	-1.57 ± 0.05	–	–	–	–	-1.74 ± 0.47
$W2$	-1.8789 ± 0.0053	-1.86 ± 0.05	–	–	–	–	-1.98 ± 0.51

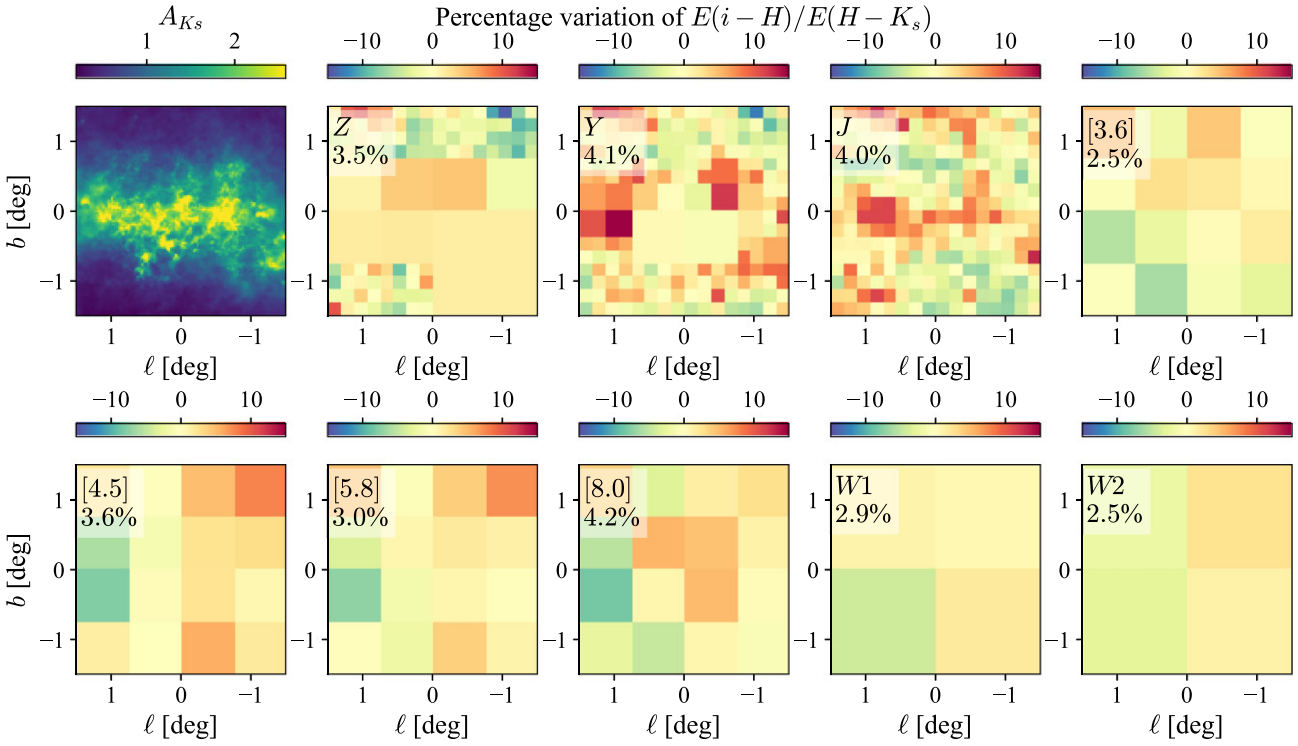

Figure 3. Percentage variation in the selective extinction ratios $E(i-H)/E(H-K_s)$. Top left shows the A_{K_s} extinction map computed using the RJCE method (see Appendix B2). Pixels are subdivided to ensure at least 500 stars per pixel. Typically variations are $\lesssim 5$ per cent.

a range of fields with different extinctions breaks the degeneracy without assuming a red clump absolute magnitude. This method shares elements with the classic method of measuring the slope of the red clump feature in colour–magnitude space (e.g. Nishiyama et al. 2009; Alonso-García et al. 2017; Nogueras-Lara et al. 2018) and is very similar to the methods of Matsunaga et al. (2016) and Dékány et al. (2019) who considered what the extinction law could plausibly be to put a group of Cepheids at the Galactic centre.

3.1 Model

We only consider stars within $11.5 < K_{s0} < 14.5$, and if J and H are available additional colour cuts of $0.2 - 1.5\sigma_{JK} < (J-K_s)_0 < 1 + 1.5\sigma_{JK}$ and $-0.3 - 1.5\sigma_{HK} < (H-K_s)_0 < 0.5 + 1.5\sigma_{HK}$ (initially using the Alonso-García et al. 2018 extinction curve) and the extinction spreads σ_i estimated from the red clump method (see Appendix B1). We initially bin the sky in Healpix with NSIDE = 128 and subdivide until all bins have no fewer than 5000 stars. We define our model of the extinction-corrected magnitude distribution for an on-sky bin (ℓ, b) as

$$
\begin{aligned}
p(K_{s0}) &= wM(K_{s0}) + (1-w)B(K_{s0}),\\
M(K_{s0}) &= N_M^{-1}\mathcal{C}(K_{s0}) \int \mathrm{d}K'_{s0}\mathcal{N}(K_{s0}|K'_{s0},\sigma_{K_s})M_0(K'_{s0}),\\
M_0(K'_{s0}) &= \exp\left(\frac{3\ln 10 K'_{s0}}{5}\right) \sum_{i=1}^{i=N_G} \omega_i \mathcal{N}(K'_{s0}|\mu_{i,K_s}, \Sigma_{i,K_s}),\\
B(K_{s0}) &= N_B^{-1}\left(1 + aK_{s0} + bK_{s0}^2\right),\\
\mathcal{N}(x|\mu,s) &= \frac{1}{\sqrt{2\pi s^2}} \exp\left(-\frac{(x-\mu)^2}{2s^2}\right).
\end{aligned}
\tag{7}
$$

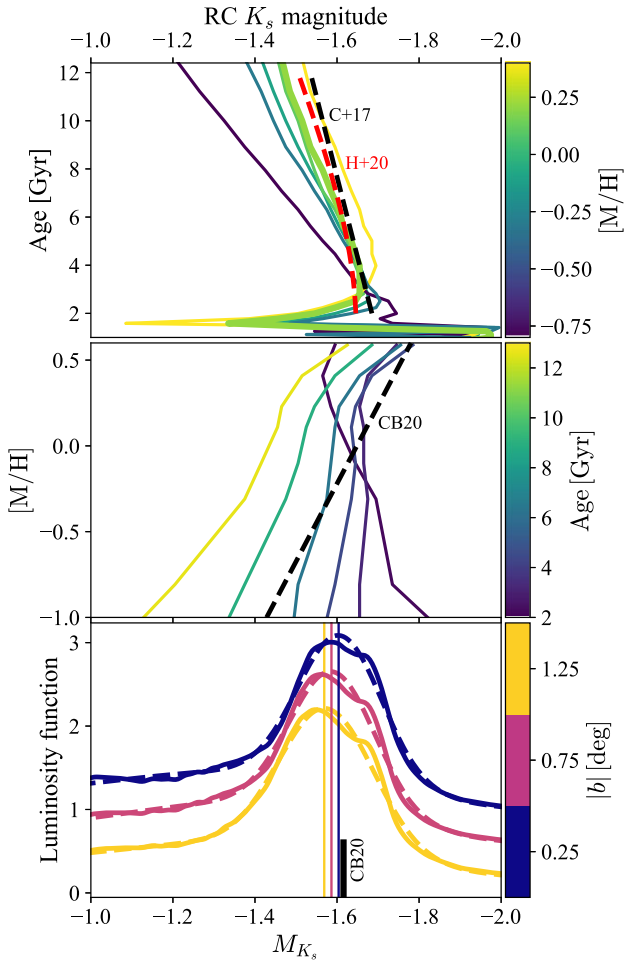

Figure 4. Properties of the red clump from PARSEC isochrones. The top panel shows the peak of the red clump distribution as a function of age coloured by metallicity. Two observational results are overplotted from Chen et al. (2017, C + 17) and Huang et al. (2020, H + 20) in black and red dashed, respectively. The middle panel shows similar but as a function of metallicity coloured by age with the observational result from Chan & Bovy (2020, CB20) overplotted. The bottom panel shows the luminosity function for all giant stars (solid lines) coloured by Galactic latitude computed using an approximate star formation history from Bernard et al. (2018) and spectroscopic metallicity distributions from a collection of sources (see the text). The distributions are vertically offset for clarity. The dashed lines show a fit using two Gaussians (red clump and red giant branch bump) plus a quadratic (red giants). The vertical lines show the mean of the Gaussian fitted to the red clump. The black line is the solar neighbourhood result from Chan & Bovy (2020).

Our model is a mixture of a background quadratic model, B, summed with one or two components, M, which represent the red clump and red giant branch bumps. The density models of red clump and red giant branch bump stars are Gaussians $\mathcal{N}(K'_{s0} - \mu_{i,K_s}, \Sigma_{i,K_s})$ which are transformed to magnitude space with the Jacobian $\exp(\frac{3\ln 10 K'_{s0}}{5})$. We convolve these magnitude distributions with a Gaussian of width σ_{K_s} which is the quadrature sum of the intrinsic magnitude spread of the red clump (Chan & Bovy 2020), the extinction spread and the median magnitude error. $\mathcal{C}^{-1}(K_{s0})$ is the completeness at unextincted magnitude K_{s0} found by interpolating unextincted magnitude against completeness, which is a function of extincted magnitude, for the stars in each on-sky bin. The completeness analysis is presented in Appendix C. The normalization factors N_M and N_B are the model and background integrated over the magnitude range. For speed, we evaluate $M(K_{s0})$ on a grid and interpolate for each star as well as the normalization integrals.

For each on-sky bin, we initially extinction correct K_s using the red clump and Rayleigh Jeans colour excess method maps described in Appendix B1 and Appendix B2. $E(H - K_s)_{\rm RC}$ is used if $A_{K_s} < 2$ and $E(H - [4.5])$ otherwise as it is more reliable in high extinction regions where the red clump stars around the Galactic centre are so heavily extincted they are lost in VIRAC2 H. We use the extinction law computed from the previous section combined with Alonso-García et al. (2018) to find $R_{H-[4.5]} = A_{K_s}/E(H - [4.5])$. Although 2D extinction maps neglect the extinction variation along the line-of-sight, they should accurately capture the extinction to the peak stellar density so on the average should correctly estimate the extinction to the bulge/nuclear stellar disc populations. As a compromise to this, Nogueras-Lara, Schödel & Neumayer (2021) consider the dust as composed of two layers but the second layer corresponds to the peak stellar density. This 'dust-screen' model could introduce biases for significant line-of-sight extinction variation through the bulge region, which we account for later in a model variant.

We then fit the model by maximizing the log-likelihood for a model with one or two Gaussians and take that with the lower Akaike information criterion. We fit the parameters $a, b, \mu_{i,K_s}, \Sigma_{i,K_s}, \omega_i, w$. The parameter of interest is μ_{0,K_s} which gives the peak unextincted apparent magnitude of the red clump. Note that this value is distinct from the peak of the magnitude distribution as we will discuss shortly. We then compute the expected μ_{0,K_s}, μ'_{0,K_s}, from an assumed red clump absolute magnitude $M_{K_s,\rm RC}$ and distance to the population of (8.275 ± 0.034) kpc (Gravity Collaboration 2021). Note that the uncertainty in distance modulus to the Galactic centre is ~ 0.01 mag which is smaller than the uncertainty on the red clump magnitude, which we will discuss later. However, this rests on the assumption that the density structure of the Galaxy on scales of ~ 1 deg peaks at the location of Sgr A∗. This is supported by evidence that it is the dynamical centre of the Galaxy from the kinematics of the bulge (Sanders et al. 2019; Clarke & Gerhard 2022), the nuclear stellar disc (Schönrich, Aumer & Sale 2015; Sormani et al. 2022) and gas kinematics (e.g. Sormani, Binney & Magorrian 2015). For each on-sky bin, we compute $\Delta\mu = \mu_{0,K_s} - \mu'_{0,K_s}$ and calculate an updated $R_{H-[4.5]} \leftarrow (1 + \Delta\mu/\langle A_{K_s}\rangle)R_{H-[4.5]}$. We repeat the entire procedure a further two times using the updated extinction law (including generating the utilized sample which depends on the choice of extinction law). Systematic errors in μ_{0,K_s} translate into systematic errors in $R_{H-[4.5]}$ as $\Delta R_{H-[4.5]} = \Delta\mu_{0,K_s}/\langle E(H - [4.5])\rangle$.

It is worth briefly considering how the mode of the magnitude distribution varies with the distribution of the red clump stars. Assuming all red clump stars have the same absolute magnitude, $M_{\rm RC}$, and trace a Gaussian density distribution $\rho(\boldsymbol{x}) = \mathcal{N}(\boldsymbol{x} - \boldsymbol{x}_0, \sigma)$, the observed unextincted magnitude distribution is

$$p(K_s) = s^3\rho(\boldsymbol{x}) \approx s^3\mathcal{N}(s - s_0, \sigma), \tag{8}$$

for lines of sight close to the Galactic centre, which is a distance s_0 away. Here $K_s = M_{\rm RC} + 5\log_{10}(100s/\text{kpc})$. Note that although the peak of the density distribution is at $K_s = K_{s,\rho} = M_{\rm RC} + 5\log_{10}(100s_0/\text{kpc})$, the peak of the magnitude distribution is at $K_s \approx K_{s,\rho} + 3(5/\ln 10)\sigma^2/s_0^2$ (assuming $\sigma/s_0 \ll 1$). This means intrinsically broader density distributions will have fainter peaks in the magnitude distribution. For instance, a density distribution of width 1(2) kpc would give rise to a magnitude shift of $\sim 0.1(0.4)$ mag. Without proper modelling this would result in a larger inferred distance of $\Delta s = 3\sigma^2/s_0$ (so $\sim 0.4(1.5)$ kpc for our example). Note

Table 2. Measurements of the absolute extinction ratio $R_{H-[4.5]}$. Each row corresponds to a different model. The columns display (i) $R_{H-[4.5]}$ assuming a reference $M_{K_s,\mathrm{RC}}$ (-1.622 for all models except (b)), (ii) $R_{H-[4.5]}$ only for $|b| < 0.2$ deg, (iii) the gradient of $R_{H-[4.5]}$ with ℓ, (iv) the gradient of $R_{H-[4.5]}$ with $|b|$, (v) the gradient of $R_{H-[4.5]}$ with A_{K_s}, (vi) the near-IR extinction law slope measured from A_J/A_H (α_{JH}), (vii) the near-IR extinction law slope measured from A_H/A_{K_s} (α_{HK}), (vii) the choice of $M_{K_s,\mathrm{RC}}$ which minimizes the spread in $R_{H-[4.5]}$ with the error given by the uncertainty in $R_{H-[4.5]}$ divided by the gradient of $R_{H-[4.5]}$ with $M_{K_s,\mathrm{RC}}$, and (viii) $R_{H-[4.5]}$ at this $M_{K_s,\mathrm{RC}}$. The set of models are (a) our fiducial model with no vertical magnitude gradient, a width of the red clump of 0.11 mag and a combination of both $(H-K_s)_{\mathrm{RC}}$ and $(H-[4.5])$ for extinction in low and high extinction regions, respectively, (b) using a red clump absolute magnitude gradient of $\mathrm{d}M_{K_s,\mathrm{RC}}/\mathrm{d}|b| = 0.03\,\mathrm{mag\,deg^{-1}}$, (c) extinction just using $(H-K_s)_{\mathrm{RC}}$, (d) extinction just using $(H-[4.5])$, (e) assuming the distribution of stars is aligned with the bar, (f) using an increased number of stars per bin and (g) accounting for a linear gradient of extinction with distance.

Model	(i) $R_{H-[4.5]}$	(ii) $R_{\lvert b\rvert<0.2}$	(iii) $\partial_\ell R$	(iv) $\partial_{\lvert b\rvert} R$	(v) $\partial_{M_{K_s}} R$	(vi) α_{JH}	(vii) α_{HK_s}	(viii) $M_{K_s,\mathrm{RC}}$	(ix) R_{min}
(a) Fiducial	0.700 ± 0.034	0.678 ± 0.036	−0.009	+0.033	−0.531	−2.22 ± 0.08	−2.14 ± 0.08	−1.605 ± 0.065	0.690 ± 0.037
(b) Vertical gradient	0.690 ± 0.037	0.669 ± 0.027	−0.016	−0.006	−0.527	−2.23 ± 0.09	−2.16 ± 0.09	−1.641 ± 0.063	0.702 ± 0.038
(c) $E(H-K_s)$	0.704 ± 0.034	0.689 ± 0.034	−0.010	+0.034	−0.535	−2.22 ± 0.08	−2.13 ± 0.08	−1.609 ± 0.065	0.695 ± 0.036
(d) $E(H-[4.5])$	0.702 ± 0.038	0.667 ± 0.028	−0.006	+0.021	−0.538	−2.22 ± 0.09	−2.13 ± 0.09	−1.609 ± 0.067	0.693 ± 0.038
(e) Bar angle	0.706 ± 0.047	0.673 ± 0.047	+0.042	+0.057	−0.531	−2.21 ± 0.11	−2.13 ± 0.11	−1.571 ± 0.076	0.669 ± 0.041
(f) Coarser resolution	0.694 ± 0.037	0.671 ± 0.021	+0.007	+0.045	−0.473	−2.22 ± 0.09	−2.14 ± 0.09	−1.593 ± 0.060	0.679 ± 0.041
(g) Extinction gradient	0.711 ± 0.037	0.689 ± 0.036	−0.007	+0.038	−0.539	−2.21 ± 0.09	−2.11 ± 0.08	−1.603 ± 0.067	0.698 ± 0.038

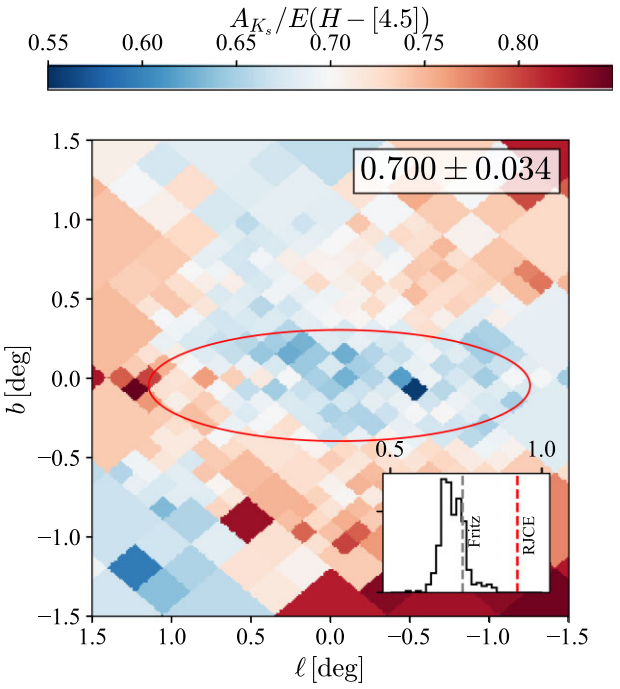

Figure 5. Variation of $R_{H-[4.5]} = A_{K_s}/E(H-[4.5])$ across the central $3 \times 3\,\mathrm{deg}^2$ assuming a fixed red clump magnitude of $M_{K_s,\mathrm{RC}} = -1.622$. The ellipse gives the approximate extent of the nuclear stellar disc. The inset plot displays the distribution of values along with other measurements.

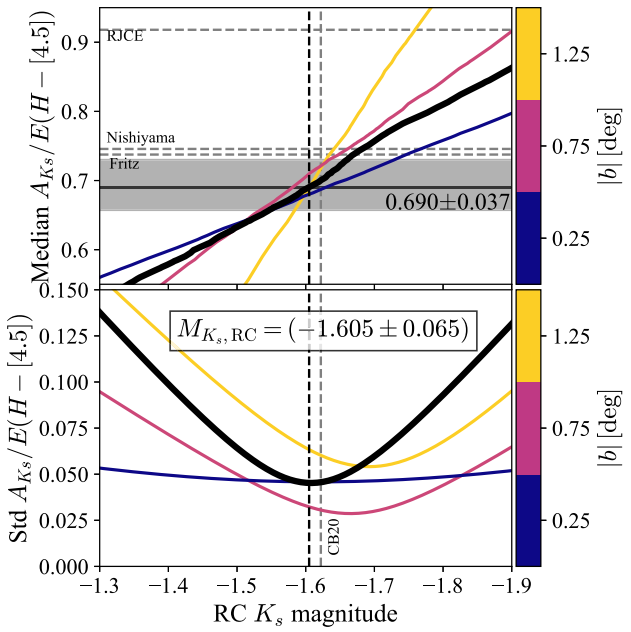

Figure 6. Results of fitting the red clump density peak. The top panel shows the variation of $R_{H-[4.5]} = A_{K_s}/E(H-[4.5])$ with the assumed red clump absolute magnitude. The coloured lines show the median computed over different on-sky regions as shown in the colour bar. The solid black is for the entire region. The horizontal dashed lines show the measurements from other authors. The second panel shows the standard deviation of $A_{K_s}/E(H-[4.5])$. The absolute magnitude of the red clump at the minimum standard deviation in $A_{K_s}/E(H-[4.5])$ is marked as a black dashed line. The horizontal band in the upper panel gives the median $A_{K_s}/E(H-[4.5])$ and $\pm 1\sigma$ computed over on-sky pixels for this choice of red clump magnitude.

that neither broadening from magnitude uncertainties, nor the width of the red clump nor extinction give rise to this effect.

3.1.1 Red clump properties

Red clump stars are the low mass helium burning stage of stellar evolution. Girardi (2016) reviews the properties of red clump stars as well as their use as distance and extinction tracers. In stars with initial masses below $\sim 1.5\,M_\odot$, the post-main sequence core is electron-degenerate. During hydrogen shell burning on the giant branch the core accretes until a core mass of around $0.5\,M_\odot$ is reached and the electron degeneracy is lifted through a series of He flashes. This produces a core mass independent of initial mass and hence gives rise to the standard candle nature. In higher mass stars, electron degeneracy is not reached in the core and core He burning proceeds after the main sequence producing a monotonic relationship between core and initial mass, giving rise to secondary red clump stars, a fainter extension of the red clump. Despite the near constancy of the core mass, variations in the absolute magnitude of red clump stars occur due to metallicity and age variations, although these tend to be minimized in the K_s band. Girardi (2016) also highlights that, even at fixed age and metallicity, the skew of the magnitude distribution of

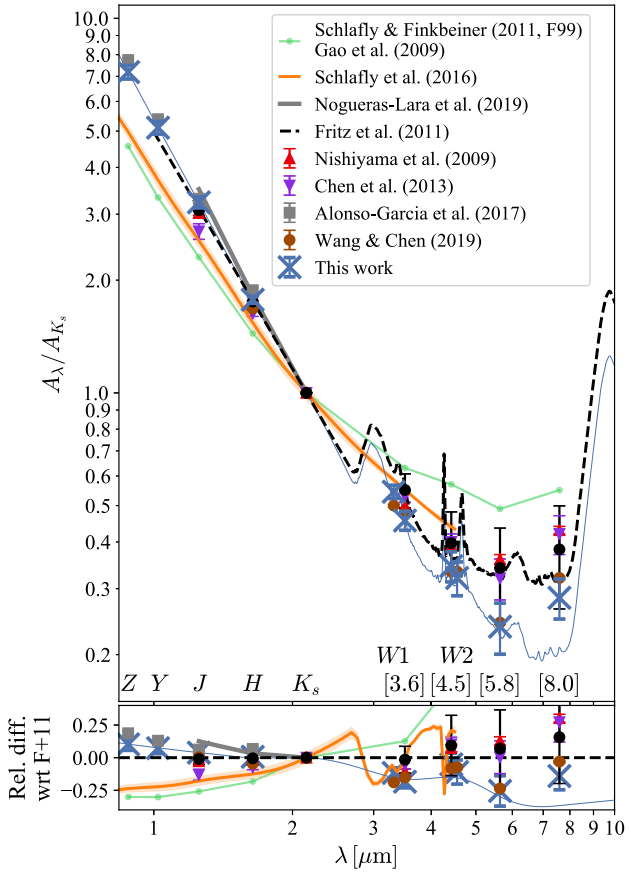

Figure 7. Our measured extinction curve (blue crosses and the monochromatic approximation from Table 4 in thin blue) alongside other literature measurements (all corresponding to the Galactic centre/Galactic bulge region except Gao, Jiang & Li 2009, Schlafly & Finkbeiner 2011 that uses the Fitzpatrick 1999 law and Schlafly et al. 2016). The errorbar combines the uncertainty in the selective extinction ratios from fitting the entire region and the variation in $R_{H-[4.5]} = A_{Ks}/E(H-[4.5])$ across the region. The lower panel shows the relative residual with respect to the Fritz et al. (2011) extinction curve (black dashed top panel).

the red clump can be significant, although the distribution becomes more symmetric for older populations.

In Fig. 4 we show the properties of the peak of the red clump K_s magnitude distribution as a function of age and metallicity for a set of PARSEC isochrones (Bressan et al. 2012; Chen et al. 2014, 2015; Tang et al. 2014; Marigo et al. 2017). Below ~ 2 Gyr 'red clump' stars burn helium in non-degenerate conditions giving rise to significant variation in the luminosity with mass and producing the so-called secondary clump. Above this age, the behaviour of the absolute magnitude of the red clump stars is more constant. The older, lower mass stars tend to be fainter than their younger counterparts, a trend that steepens for more metal-poor stars. Both Chen et al. (2017) and Huang et al. (2020) have provided calibrations for $M_{K_s,\mathrm{RC}}$ as a function of age via asteroseismic measurements (here we use the calibration for [Fe/H]>0.1 from Huang et al. 2020), which match well the behaviour of the PARSEC isochrones with a typical gradient of ~ 0.015 mag Gyr^{-1}. It should be noted however that the age distribution of red clump stars are known to not trace the underlying star formation history. Bovy et al. (2014) shows how for a flat star formation history the red clump age distribution is strongly skewed towards young stars with a mode around 2 Gyr. Therefore, even for star formation histories biased to early star formation the mean red clump age will be significantly smaller than the peak star formation epoch (provided star formation is not strongly truncated at early times). Fig. 4 also shows how typically the red clump K_s magnitude becomes brighter for more metal-rich populations with the gradient steepening for older populations. The gradient for the PARSEC isochrones for older populations agrees well with the gradient of -0.21 mag dex^{-1} found from Chan & Bovy (2020) using APOGEE and Gaia DR2 data. Chan & Bovy (2020) also show how there is a magnitude gradient with [α/Fe] for the APOGEE stars of ~ 0.33 mag dex^{-1}. Combining with the asteroseismic measurements, a gradient of [α/Fe] with age of ~ 0.05 dex Gyr^{-1} would produce such an effect. This is typically the gradient observed in the solar neighbourhood (Feuillet et al. 2019). Therefore, it is unclear observationally what role alpha-enhancement plays in altering the red clump magnitude.

3.1.2 *Red clump distribution in the inner Galaxy*

With the theoretical and observational considerations of the previous section, we now turn to predicting the expected behaviour of the red clump magnitude for the considered sample of stars. The metallicity distribution of the inner Galaxy has been revealed through several spectroscopic surveys e.g. ARGOS (Ness et al. 2013), APOGEE (Rojas-Arriagada et al. 2020), GES (Rojas-Arriagada et al. 2014), and GIBS (Zoccali et al. 2017). The results from these surveys are in agreement that the metallicity distribution of the inner Galaxy consists of multiple sub-components (Ness et al. 2013) and that there is a vertical metallicity gradient (Gonzalez et al. 2013). In the inner 3×3 deg^2 there are comparatively few spectroscopic studies outside of the NSC. The most recent data is summarized by Schultheis et al. (2019). We have taken stellar metallicity data from APOGEE DR16 (Ahumada et al. 2020), Nandakumar et al. (2018), and GIBS (Zoccali et al. 2014, 2017). This sample has mean metallicity -0.07 dex and standard deviation ~ 0.4 dex. The mean [Fe/H] is -0.18 dex. In [α/Fe] versus [Fe/H], the distribution follows a standard chemical evolution track with the metal-rich stars not displaying any α-enhancement (possibly even a small α deficit). The metallicity distribution is clearly composed of a metal-rich and metal-poor component, the latter of which becomes more dominant at higher latitudes giving rise to a metallicity gradient of -0.1 dex/deg.

The age distribution of the inner Galaxy is less well known. Traditionally, from photometry, the bulge has been viewed as an old structure (e.g. Zoccali et al. 2003) but this was thrown into question by spectroscopic ages of microlensed dwarfs (Bensby et al. 2013), many of which are young. Recent work by Bernard et al. (2018) constrained the age distribution of the bulge (-5 deg $\lesssim b < -2$ deg) from *Hubble Space Telescope* photometry of the main sequence turn-off stars, concluding that, although the bulge is predominantly old, approximately 10 per cent of stars are younger than 5 Gyr. This fraction increases to ~ 20 per cent for more metal-rich ([Fe/H] $\gtrsim 0.2$ dex) stars, consistent with the Bensby et al. (2013) work. Further evidence for a predominantly old ($\gtrsim 8$ Gyr) bulge comes (indirectly) from [C/N] measurements of giant stars (Bovy et al. 2019; Hasselquist et al. 2020), although, as highlighted by Hasselquist et al. (2020), age appears to correlate with both metallicity and Galactic height of the populations. Nogueras-Lara et al. (2020a) have used the luminosity of red clump stars to conclude the majority (~ 95 per cent) of the nuclear stellar disc formed more than 8 Gyr ago with some evidence of a more recent (< 1 Gyr ago) star formation burst (Matsunaga et al. 2011). This is consistent with ongoing/recent star formation within the central molecular zone (Morris & Serabyn 1996) and is

Table 3. Derived extinction law using $R_{H-[4.5]} = (0.700 \pm 0.034)$ from the fiducial model in Table 2. Here we have combined the colour excess measurements with the absolute extinction measurement, and we compare to pre-existing measurements (we quote the Fritz et al. 2011 results for a 9480 K spectrum but the dependence on the source spectrum is weak). The first uncertainty comes from combining the uncertainty in the colour ratios fitted over the whole region (essentially negligible) together with the variance in $R_{H-[4.5]}$ across the region, whilst the second is the contribution from the variance in the colour ratios across the region. Note that Nishiyama et al. (2009) report coefficients for the SIRIUS bands, Wang & Chen (2019) for the 2MASS bands and Nogueras-Lara et al. (2019a) for the HAWK-I bands (see the end of Section 2.2 for approximate conversions). For each band, x, we report the effective wavelength $\lambda_{\rm eff} = \int {\rm d}\lambda\, T_x(\lambda) F_\lambda(\lambda) \lambda^2 / \int {\rm d}\lambda\, T_x(\lambda) F_\lambda(\lambda) \lambda$ using a Castelli & Kurucz (2003) $T_{\rm eff} = 4750$ K spectrum F_λ.

Band	$\lambda_{\rm eff}$ (nm)	A_x/A_{K_s}	Fritz et al. (2011)	Alonso-García et al. (2017)	Nishiyama et al. (2009)	Nogueras-Lara et al. (2019a)	Wang & Chen (2019)
Z	879.583	$7.19 \pm 0.30 \pm 0.19$	–	7.74 ± 0.11	–	–	–
Y	1021.237	$5.11 \pm 0.20 \pm 0.14$	4.64 ± 0.22	5.38 ± 0.07	–	–	–
J	1252.522	$3.23 \pm 0.11 \pm 0.06$	3.07 ± 0.13	3.30 ± 0.04	3.02 ± 0.04	3.51 ± 0.04	3.12 ± 0.17
H	1639.371	$1.77 \pm 0.04 \pm 0.04$	1.75 ± 0.08	1.88 ± 0.03	1.73 ± 0.03	1.81 ± 0.01	1.68 ± 0.11
[3.6]	3508.050	$0.46 \pm 0.03 \pm 0.03$	0.55 ± 0.06	–	0.50 ± 0.01	–	0.47 ± 0.05
[4.5]	4421.765	$0.34 \pm 0.03 \pm 0.05$	0.40 ± 0.08	–	0.39 ± 0.01	–	0.33 ± 0.04
[5.8]	5641.275	$0.24 \pm 0.04 \pm 0.05$	0.34 ± 0.09	–	0.36 ± 0.01	–	0.24 ± 0.04
[8.0]	7591.510	$0.28 \pm 0.03 \pm 0.06$	0.38 ± 0.12	–	0.43 ± 0.01	–	0.32 ± 0.04
$W1$	3317.236	$0.54 \pm 0.02 \pm 0.03$	–	–	–	–	0.50 ± 0.06
$W2$	4552.394	$0.32 \pm 0.03 \pm 0.04$	–	–	–	–	0.33 ± 0.05

Table 4. A portion of the provided approximation to the monochromatic extinction law normalized with respect to the extinction at the K_s effective wavelength (2.144 μm).

Wavelength (μm)	$A(\lambda)/A(2.144\ \mu{\rm m})$
0.800000	8.952603
0.800920	8.928876
0.801840	8.905239
...	...
9.999080	1.181260
10.000000	1.181112

broadly consistent with the conclusions of Bernard et al. (2018) on the wider bar/bulge but possibly suggesting the nuclear stellar disc is on average older than the surrounding bulge. We have fitted by-eye a very simple star formation history to the 'cleanest' combined fit from Bernard et al. (2018) of the form $\mathrm{sech}^2((13.5\,{\rm Gyr} - \tau)/4.7\,{\rm Gyr})$ with a truncation at 14 Gyr. Combining the metallicity distributions and star formation histories with the PARSEC isochrones and adopting a Kroupa (2001) initial mass function, we have computed the luminosity function of the giant branch stars in the inner bulge region. We show the results in the lower panel of Fig. 4 along with a simple double Gaussian plus quadratic fit to represent the red clump stars, the red giant branch bump stars and the red giant branch stars respectively. We find that the lowest latitude bin has a red clump magnitude of $M_{K_s,{\rm RC}} = -1.61$ mag. This agrees well with the mean solar neighbourhood result from Chan & Bovy (2020) of $M_{K_s,{\rm RC}} = -1.622$ mag and more specifically using their relations adopting the mean $(J - K_s) = 0.647$ (see Appendix B1) and mean metallicity -0.18 dex gives $M_{K_s,{\rm RC}} = -1.595$ mag. The metallicity gradient with latitude produces a red clump magnitude gradient of 0.032 mag deg^{-1} whilst using the change in mean metallicity in combination with the results of Chan & Bovy (2020) we would expect 0.024 mag deg^{-1}. At all latitudes the red clump distribution is well reproduced by a Gaussian with standard deviation ~ 0.11 mag. Chan & Bovy (2020) measured the solar neighbourhood red clump to have an intrinsic standard deviation of 0.097 mag which combined in quadrature with that arising from the metallicity variance predicts a standard deviation of ~ 0.13 mag, similar to the PARSEC models. The red clump peaks from the PARSEC isochrones have a slight bimodal structure arising from the bimodal metallicity distributions such that the mode typically peaks ~ 0.03 mag fainter than the Gaussian mean.

3.2 Results

We apply the method described in the previous subsection using different assumptions for the red clump distribution. All results are given in Table 2. As our fiducial model we use the absolute K_s magnitude from Chan & Bovy (2020) of $M_{K_s,{\rm RC}} = -1.622$. Chan & Bovy (2020) derived the absolute magnitude using 2MASS data. The K_s bands in VVV and 2MASS differ according to $K_{s,\,{\rm VVV}} = K_{s,\,2{\rm MASS}} + 0.01(J - K_s)_{2{\rm MASS}}$ (González-Fernández et al. 2018) so the difference is negligible for red clump stars with $(J - K_s) \approx 0.6$. As discussed in the previous section, the expectation from stellar models is within ~ 0.02 mag of this $M_{K_s,{\rm RC}}$. We use $\sigma_{K_s} = 0.11$ mag as the intrinsic red clump spread (consistent with the PARSEC isochrones and the expectation from Chan & Bovy (2020)). We show the resulting on-sky $R_{H-[4.5]} = A_{K_s}/E(H - [4.5])$ map in Fig. 5. We find that on average $R_{H-[4.5]} = (0.700 \pm 0.034)$ where the errorbar is from the standard deviation across inspected Healpix. The variation of ~ 5 per cent is similar to the variation in the colour excess ratios. Our value of $R_{H-[4.5]}$ can be compared to the results from Fritz et al. (2011) of $R_{H-[4.5]} = (0.74 \pm 0.06)$ and Wang & Chen (2019) of $R_{H-[4.5]} = (0.74 \pm 0.06)$. This ratio is used in the Rayleigh Jeans colour excess method (see Appendix B2) for which Majewski et al. (2011) use $R_{H-[4.5]} = 0.918$ based on the extinction laws from Indebetouw et al. (2005). We see some clear correlated structure in Fig. 5: most obviously the mid-plane within the nuclear stellar disc has lower $R_{H-[4.5]}$. This might imply a fainter red clump magnitude in this region possibly reflecting a star formation history more biased towards earlier times (Nogueras-Lara et al. 2020a). In Fig. 6 we show the median of $R_{H-[4.5]}$ as a function of the assumed red clump $M_{K_s,{\rm RC}}$. The slope of $R_{H-[4.5]}$ with red clump magnitude reflects the mean extinction. Lower extinction leads to steeper slopes. This means constraints from lower latitude bins are more trustworthy as they are less reliant on assumptions regarding the red clump magnitude.

Instead of assuming a magnitude for the red clump, we can assume the extinction coefficient $R_{H-[4.5]}$ is constant over the inspected region. Due to the range of slopes in the top panel of

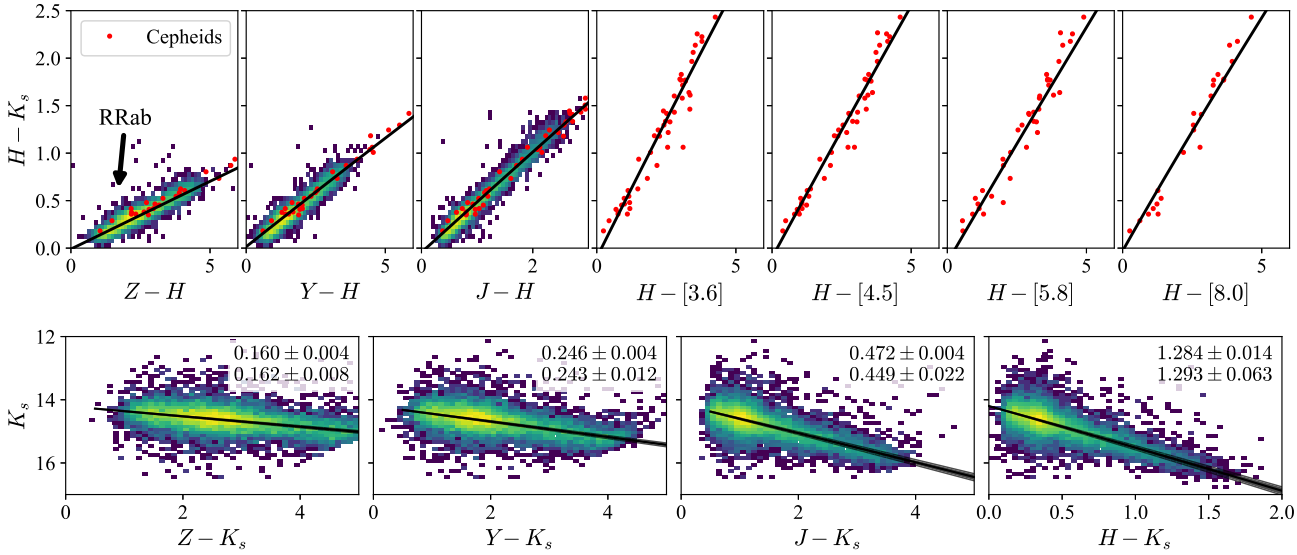

Figure 8. Colour–colour (upper) and colour–magnitude (lower) diagrams for Cepheids (red points) and RR Lyrae ab (histogram) with the derived extinction law overplotted. The reported numbers in the lower panels are the slope measured from the RR Lyrae ab sample (upper) and measured in this paper (lower).

Fig. 6 there is a choice of red clump magnitude that reduces the spread in $R_{H-[4.5]}$. In the lower panel of Fig. 6 we show the standard deviation of $R_{H-[4.5]}$ as a function of $M_{K_s,\mathrm{RC}}$. The minimum occurs at $M_{K_s,\mathrm{RC}} = -1.605$ where $R_{H-[4.5]} = (0.690 \pm 0.037)$. We derive an uncertainty in $M_{K_s,\mathrm{RC}}$ by fixing $R_{H-[4.5]} = 0.690$ and finding the resultant spread in $M_{K_s,\mathrm{RC}} = 0.065$. This gives us a best estimate for the inner bar/bulge red clump absolute K_s magnitude as (-1.61 ± 0.07) mag. This agrees well with the expectation of $M_{K_s,\mathrm{RC}} = -1.595$ from the Chan & Bovy (2020) models when adjusted for the mean colour and metallicity (and other results from Alves 2000; Laney, Joner & Pietrzyński 2012; Chen et al. 2017; Hawkins et al. 2017; Ruiz-Dern et al. 2018; Hall et al. 2019) and gives good evidence of the standard candle nature of the red clump across a range of Galactic environments. Combining with the mean red clump colour measurements from Appendix B1 we find $M_{J,\mathrm{RC}} = (-0.96 \pm 0.06)$ mag and $M_{H,\mathrm{RC}} = (-1.46 \pm 0.06)$ mag.

In addition to the fiducial model, we also run some model variants to inspect any possible systematic uncertainty in our results. Based on the discussion of the previous subsection, we run a model with a gradient of the magnitude of the red clump with latitude ((b) in Table 2). We opt for $\mathrm{d}M_{K_s,\mathrm{RC}}/\mathrm{d}|b| = 0.03\,\mathrm{mag\,deg^{-1}}$ which agrees approximately with the results from the PARSEC isochrones and the expectation from the results of Chan & Bovy (2020). As expected, we find a slightly lower $R_{H-[4.5]} = (0.690 \pm 0.037)$ reflecting the gradient of $R_{H-[4.5]}$ with latitude seen in Fig. 5. Minimizing the spread of the red clump magnitude (accounting for the vertical gradient) leads to $M_{K_s,\mathrm{RC}} = (-1.641 \pm 0.063)$ demonstrating the red clump in the Galactic centre may be ∼0.02 magnitudes brighter than the fiducial solar neighbourhood value possibly as it is more metal-rich (e.g. see Schultheis et al. 2019). However, all of these results are still consistent with our fiducial model within the reported uncertainties. We run a further two model variants ((c) and (d) in Table 2) where we solely use the $E(H-K_s)$ extinction maps from the red clump method or solely the $E(H-[4.5])$ extinction maps from all giant branch stars. The differences with respect to the fiducial model are negligible. As we only consider sources within 1.5 deg of the Galactic centre, the magnitude gradient due to the bar introduces shifts of ∼ 0.1 mag assuming a bar angle of 28 deg. However, many of the observed stars are expected to be part of the nuclear stellar disc, the geometry of which is poorly known although Sormani et al. (2022) demonstrated an axisymmetric dynamical model gives a good representation of the currently quite limited data. Running a model using a non-zero bar angle ((e) in Table 2) does not produce any significant difference in $R_{H-[4.5]}$. We run a model ((f) in Table 2) with a coarser graining of the HEALPIX initially using NSIDE = 64 and subdividing requiring at least 50 000 stars per bin. Again, this does not produce any significant difference. A final consideration is that the use of the 2d extinction maps assumes that the peak of the colour distribution corresponds to the extinction for stars at the peak density in the bulge. However, significant line-of-sight variation of the extinction through the bulge may skew the mean estimates. Using the fractional gradient of the $E(H-K_s)$ Schultheis et al. (2014) maps with distance (in kpc) averaged over each on-sky bin, $\langle(1/E(H-K_s))\mathrm{d}E(H-K_s)/\mathrm{d}s\rangle$, we find that the mean A_{Ks} extinction is too large by a factor $2(8.275\,\mathrm{kpc})(\ln 10/5)^2\Sigma^2_{K_s}\langle(1/E(H-K_s))(\mathrm{d}E(H-K_s)/\mathrm{d}s)\rangle$, where Σ_{K_s} is the fitted width of density distribution in magnitude space (this formula arises through similar considerations to the discussion of the shift of the mode magnitude below equation (8)). After fitting the parameters of the model at each iteration, we correct $\Delta\mu$ and $\langle A_{K_s}\rangle$ in each on-sky bin by this overestimate. The results are shown as model (g) of Table 6 where $R_{H-[4.5]}$ must be slightly larger than the fiducial case to compensate for the reduced A_{K_s} but the results are all comfortably within the fiducial uncertainties. More complicated dust distributions along the line-of-sight could give rise to more complicated behaviour but this gives confidence that it is a relatively weak effect.

Using $R_{H-[4.5]} = (0.700 \pm 0.034)$ in combination with the results from Table 1 we plot the resultant extinction law in Fig. 7 and give the ratios A_x/A_{K_s} in Table 3. As found by other authors, the bulge extinction law is steeper than the more typical disc Milky Way extinction law from e.g. Schlafly & Finkbeiner (2011) who give coefficients from a Fitzpatrick (1999) extinction law and Schlafly et al. (2016) who utilized APOGEE data. We find A_J/A_{K_s} and A_H/A_{K_s} slightly lower than that found by Alonso-García et al. (2017). The lower A_H/A_{K_s} is more in agreement with the results of Fritz et al. (2011). We reproduce the low $A_{[5.8]}/A_{K_s}$ from Chen et al. (2018). Using $\lambda_{\mathrm{eff}} = (1.25252, 1.63937, 2.14389)$ μm for J, H and K_s respectively, the logarithmic infrared extinction slope, or

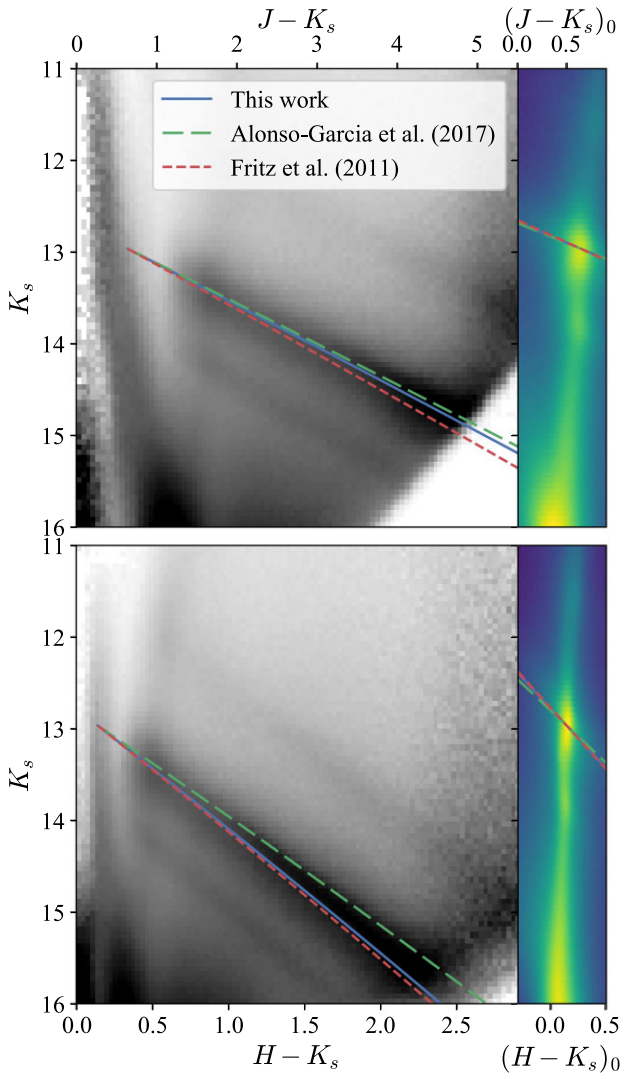

Figure 9. Colour–magnitude diagrams over the inner $3 \times 3\,\mathrm{deg}^2$ field. The greyscale shows the column-normalized density with a power-law stretch with coefficient 0.4. The extinction laws from this paper and previous works are displayed (with $\alpha_{JH} = (-2.223, -2.090, -2.088)$ and $\alpha_{HKs} = (-2.135, -2.353, -2.092)$ respectively), and the right-hand panels show the unextincted colour–magnitude diagrams. The colours show the density with a power-law stretch with coefficient 0.4.

power-law index, is found as $\alpha = (2.22 \pm 0.08)$ using the J and H bands and (2.14 ± 0.08) using the H and K_s bands. This agrees within 1σ with both the measurement from Stead & Hoare (2009) of $\alpha = (2.14 \pm 0.05)$ and the recent result of $\alpha = 2.27$ from Maíz Apellániz et al. (2020), both studies using stars across the entirety of the Galaxy but also accounting for non-linearity in the extinction calculations. This is good evidence for a near universality to the near-infrared extinction law. Hosek et al. (2018) used observations of Westerlund 1 and red clump stars in the Galactic Centre to find $\alpha = (2.38 \pm 0.15)$ whilst using integrated photometry, Stelter & Eikenberry (2021) find $\alpha = (2.03 \pm 0.06)$. Nogueras-Lara et al. (2019a) (and similar in Nogueras-Lara et al. 2020b) found evidence of a non-constant slope such that $\alpha = (2.43 \pm 0.10)$ for J, H and $\alpha = (2.23 \pm 0.03)$ for H, K_s. Our results imply a non-constant α in the same sense as these measurements although the difference we find is much smaller and within our quoted uncertainties. As seen in Fig. 5, in the mid-plane $|b| \lesssim 0.1$ deg which is the region covered by Nogueras-Lara et al. (2019a), $R_{H-[4.5]}$ is lower if the red clump magnitude is constant across the entire region we have inspected. We find $\mathrm{d}\alpha_{JH}/\mathrm{d}R_{H-[4.5]} \approx 1.3$ and $\mathrm{d}\alpha_{HK_s}/\mathrm{d}R_{H-[4.5]} \approx 2.2$. To transform Table 1 into the values of Table 3 using a different choice of $R_{H-[4.5]}$ involves

$$\frac{A_x}{A_{Ks}} = 1 + \frac{1}{1.848 R_{H-[4.5]}} \left(1 + \frac{E(H-K_s)}{E(x-H)}\right). \quad (9)$$

For ease of using the results in this paper, we provide a monochromatic approximation to the derived extinction law. We take the monochromatic extinction law, $A_{\mathrm{F11}}(\lambda)$, provided by Fritz et al. (2011) and multiply by an interpolating spline, $u(\lambda)$, with a series of nodes around the effective wavelengths of each filter considered here, and then a set beyond 15 μm with y-values of 0.7 (an arbitrary choice that approximately matches the correction required at 8 μm and ensures the gradient of the spline tends to zero at large wavelength). We then adjust the spline y-values for $\lambda < 15$ μm computing the extinction coefficient for a 4750 K spectrum using equation (1) and our adjusted extinction law, $A(\lambda) = A_{\mathrm{F11}}(\lambda)u(\lambda)$. The resulting monochromatic extinction is tabulated in Table 4 and plotted in Fig. 7.

3.3 Validation

We close with some basic tests of the results derived here. First, we inspect the colour–magnitude and colour–colour diagrams for samples of classical Cepheids and RR Lyrae ab within the inner $6 \times 6\,\mathrm{deg}^2$ (to increase number statistics) from the work of Molnar et al. (2022). These variables have been identified from the VIRAC2 catalogue using a hierarchical machine-learning classifier. We only use high-confidence variables (classification probability >0.9). The samples and the extinction vectors derived in this work are shown in Fig. 8. We find there is very good agreement between the colour–colour and colour–magnitude distributions and the corresponding extinction vectors.

Secondly, we extract a sample of VIRAC2 stars detected in at least 20 per cent of observations covering their positions and between $K_s = 11$ and $K_s = 19$. We use our 2D extinction maps to extinction correct the K_s magnitudes (assuming a fixed extinction law as reported in Table 3). The colour–magnitude diagram is shown in the left-hand panel of Fig. 9 along with a comparison of different extinction vectors. We extract two subsamples by selecting stars in two bins in unextincted magnitude: $11.2 < K_{s0} < 11.9$ corresponding to the AGB bump and $12.5 < K_{s0} < 13.3$ corresponding to the red clump. We display histograms of the resulting samples in the right-hand panels of Fig. 10. We clearly note in both samples the presence of the nuclear stellar disc which is significant for $|b| < 0.4$ deg. We overlay an ellipse with aspect ratio 0.3 which gives a good 'by-eye' match to the equi-density contours, particularly for the AGB bump sample. This agrees well with the diameter-to-thickness ratio of 5: 1 reported by Launhardt et al. (2002) based on fits to integrated NIR and FIR light, and axial ratio of 0.79 from Gallego-Cano et al. (2020). Outside of the nuclear stellar disc, there is a transition to the inner bulge, which has a rounder, yet still significantly flattened, shape.

4 CONCLUSIONS

We have measured the extinction law from 0.9 to 8 microns in the inner $3 \times 3\,\mathrm{deg}^2$ of the Galaxy. Our method involves a combination of measuring the selective extinction ratios from colour–colour diagrams of bar/bulge red giant branch stars from VVV and GLIMPSE, and measuring the absolute extinction ratio by requiring the density

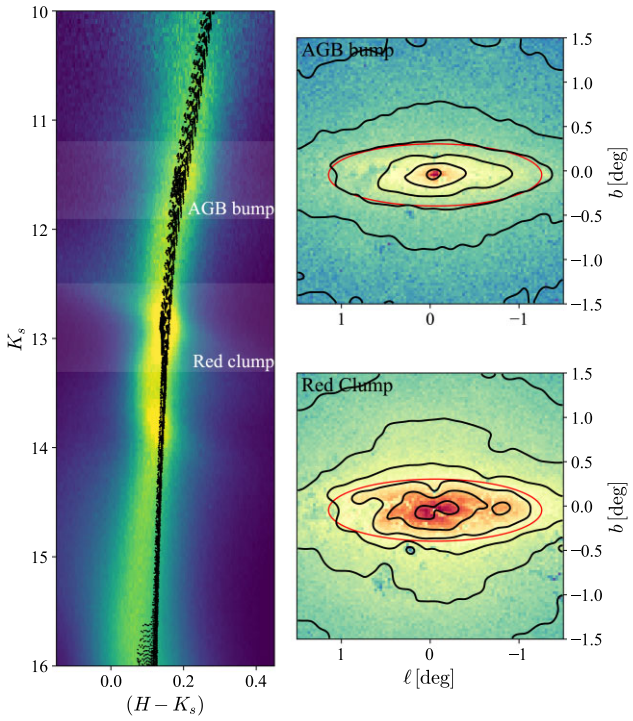

Figure 10. Number counts of stars in the nuclear stellar disc: the left-hand panel shows the unextincted $(H - K_s)$ versus K_s row-normalized colour–magnitude diagram. Solar-metallicity PARSEC isochrones with log(age/ Gyr) > 9.5 at 8.275 kpc shifted in $(H - K_s)$ by 0.05 mag are overlaid in black. The AGB bump, red clump, and red giant branch bump are clearly visible. In the right-hand panels we show the number density of stars in two K_{s0} bins around the AGB bump and red clump. We overlay a red ellipse centred on Sgr A∗ with aspect ratio 0.3.

of red clump giant stars peaks at the distance to the Galactic Centre measured by Gravity Collaboration (2021). Assuming a red clump K_s magnitude similar to that observed for stars in the solar neighbourhood, we have found that the extinction law is steep with a power-law index ($A_x \propto \lambda_x^{-\alpha}$) of $\alpha \approx 2.2$ with only a weak indication of a non-constant slope across the J, H, and K_s wavelength range. We have confirmed previous work that finds a low $A_{[5.8]}/A_{K_s} = (0.24 \pm 0.04)$. Furthermore, we have calibrated the Rayleigh-Jeans colour excess method as $A_{Ks} = 0.677(H - [4.5] - 0.188)$ for typical Galactic bulge stars with $K_s = 13$. Our work incorporates the non-linearity of the extinction with total extinction, an important effect particularly for the IRAC [8.0] band due to the 9.7 μm silicate feature. Our methods have used adaptive 2D extinction maps constructed from the mean $(J - K_s)$ and $(H - K_s)$ colours of the red clump stars and $(H - [4.5])$ of all giant stars as in high extinction regions red clump stars are too faint in J and H for VVV.

Instead of assuming a red clump K_s magnitude, we have demonstrated by ensuring the extinction law is constant over the surveyed region (as suggested by inspecting the spatial variation of the selective extinction ratios) we can independently constrain the red clump K_s magnitude as $M_{K_s,\mathrm{RC}} = (-1.61 \pm 0.07)$. Reasonable systematic variations of the fiducial model such as accounting for vertical metallicity gradients or potential asymmetries related to the bar give results consistent with this. This measurement is very similar to the mean value observed for solar neighbourhood stars and gives confidence in the use of red clump stars as standard candles throughout the Galaxy.

ACKNOWLEDGEMENTS

We thank the referee Jesús Maíz Apellániz for useful comments that improved the presentation of the work. JLS acknowledges support from the Royal Society (URF\R1\191555). DM gratefully acknowledges support by the ANID BASAL projects ACE210002 and FB210003, and by Fondecyt Project No. 1220724. This paper made used of the Whole Sky Database (wsdb) created by Sergey Koposov and maintained at the Institute of Astronomy, Cambridge by Sergey Koposov, Vasily Belokurov and Wyn Evans with financial support from the Science & Technology Facilities Council (STFC) and the European Research Council (ERC). Based on data products from observations made with ESO Telescopes at the La Silla or Paranal Observatories under ESO programme ID 179.B-2002. This research has made use of the SVO Filter Profile Service (http://svo2.cab.inta-csic.es/theory/fps/) supported from the Spanish MINECO through grant AYA2017-84089. This paper made use of NUMPY (van der Walt, Colbert & Varoquaux 2011), SCIPY (Virtanen et al. 2020), MATPLOTLIB (Hunter 2007), SEABORN (Waskom et al. 2017), and ASTROPY (Astropy Collaboration 2013; Price-Whelan et al. 2018).

DATA AVAILABILITY

All of the data used in this article are in the public domain, except for the VIRAC2 data which will be made available together with the catalogue description paper (Smith et al., in preparation). We provide the 2D extinction maps described in Appendix B1 and B2 along with code to read them at https://doi.org/10.5281/zenodo.6598900.

REFERENCES

Abdurro'uf et al., 2022, ApJS, 259, 35
Ahumada R. et al., 2020, ApJS, 249, 3
Alonso-García J. et al., 2017, ApJ, 849, L13
Alonso-García J. et al., 2018, A&A, 619, A4
Alves D. R., 2000, ApJ, 539, 732
Alves D. R., Rejkuba M., Minniti D., Cook K. H., 2002, ApJ, 573, L51
Astropy Collaboration 2013, A&A, 558, A33
Babusiaux C., Gilmore G., 2005, MNRAS, 358, 1309
Bensby T. et al., 2013, A&A, 549, A147
Bernard E. J., Schultheis M., Di Matteo P., Hill V., Haywood M., Calamida A., 2018, MNRAS, 477, 3507
Blitz L., Spergel D. N., 1991, ApJ, 379, 631
Bovy J. et al., 2014, ApJ, 790, 127
Bovy J., Leung H. W., Hunt J. A. S., Mackereth J. T., García-Hernández D. A., Roman-Lopes A., 2019, MNRAS, 490, 4740
Bressan A., Marigo P., Girardi L., Salasnich B., Dal Cero C., Rubele S., Nanni A., 2012, MNRAS, 427, 127
Castelli F., Kurucz R. L., 2003, in Piskunov N., Weiss W. W., Gray D. F., eds, Modelling of Stellar Atmospheres, Proc. 210th Symp. of IAU, Vol. 210. Astronomical Society of the Pacific, Provo, Utah, p. A20
Chan V. C., Bovy J., 2020, MNRAS, 493, 4367
Chapman N. L., Mundy L. G., Lai S.-P., Evans Neal J. I., 2009, ApJ, 690, 496
Chen Y., Girardi L., Bressan A., Marigo P., Barbieri M., Kong X., 2014, MNRAS, 444, 2525
Chen Y., Bressan A., Girardi L., Marigo P., Kong X., Lanza A., 2015, MNRAS, 452, 1068
Chen Y. Q., Casagrande L., Zhao G., Bovy J., Silva Aguirre V., Zhao J. K., Jia Y. P., 2017, ApJ, 840, 77
Chen X., Wang S., Deng L., de Grijs R., 2018, ApJ, 859, 137
Churchwell E. et al., 2009, PASP, 121, 213
Clarke J. P., Gerhard O., 2022, MNRAS, 512, 2171
Cusano F. et al., 2021, MNRAS, 504, 1

Dalton G. B. et al., 2006, in McLean I. S., Iye M., eds, Proc. SPIE Conf. Ser. Vol. 6269, Ground-based and Airborne Instrumentation for Astronomy. SPIE, Bellingham, p. 62690X
Dékány I., Hajdu G., Grebel E. K., Catelan M., 2019, ApJ, 883, 58
Dékány I., Grebel E. K., Pojmański G., 2021, ApJ, 920, 33
Emerson J. P. et al., 2004, in Quinn P. J., Bridger A., eds, Proc. SPIE Conf. Ser. Vol. 5493, Optimizing Scientific Return for Astronomy through Information Technologies. SPIE, Bellingham, p. 401
Fernique P., Boch T., Donaldson T., Durand D., O'Mullane W., Reinecke M., Taylor M., 2014, MOC - HEALPix Multi-Order Coverage map Version 1.0, IVOA Recommendation. preprint (arXiv:1505.02937)
Feuillet D. K., Frankel N., Lind K., Frinchaboy P. M., García-Hernández D. A., Lane R. R., Nitschelm C., Roman-Lopes A., 2019, MNRAS, 489, 1742
Fitzpatrick E. L., 1999, PASP, 111, 63
Fritz T. K. et al., 2011, ApJ, 737, 73
Gallego-Cano E., Schödel R., Nogueras-Lara F., Dong H., Shahzamanian B., Fritz T. K., Gallego-Calvente A. T., Neumayer N., 2020, A&A, 634, A71
Gao J., Jiang B. W., Li A., 2009, ApJ, 707, 89
García Pérez A. E. et al., 2016, AJ, 151, 144
Girardi L., 2016, ARA&A, 54, 95
Girardi L., Salaris M., 2001, MNRAS, 323, 109
Girardi L., Bertelli G., Bressan A., Chiosi C., Groenewegen M. A. T., Marigo P., Salasnich B., Weiss A., 2002, A&A, 391, 195
Gonzalez O. A., Rejkuba M., Zoccali M., Valenti E., Minniti D., 2011, A&A, 534, A3
Gonzalez O. A., Rejkuba M., Zoccali M., Valenti E., Minniti D., Schultheis M., Tobar R., Chen B., 2012, A&A, 543, A13
Gonzalez O. A., Rejkuba M., Zoccali M., Valent E., Minniti D., Tobar R., 2013, A&A, 552, A110
González-Fernández C. et al., 2018, MNRAS, 474, 5459
Gravity Collaboration 2019, A&A, 625, L10
Gravity Collaboration 2021, A&A, 647, A59
Hajdu G., Dékány I., Catelan M., Grebel E. K., 2020, Exp. Astron., 49, 217
Hall O. J. et al., 2019, MNRAS, 486, 3569
Hasselquist S. et al., 2020, ApJ, 901, 109
Hawkins K., Leistedt B., Bovy J., Hogg D. W., 2017, MNRAS, 471, 722
Hogg D. W., Bovy J., Lang D., 2010, preprint (arXiv:1008.4686)
Hosek Matthew W. J. et al., 2018, ApJ, 855, 13
Huang Y. et al., 2020, ApJS, 249, 29
Hunter J. D., 2007, Comput. Sci. Eng., 9, 90
Indebetouw R. et al., 2005, ApJ, 619, 931
Kroupa P., 2001, MNRAS, 322, 231
Laney C. D., Joner M. D., Pietrzyński G., 2012, MNRAS, 419, 1637
Launhardt R., Zylka R., Mezger P. G., 2002, A&A, 384, 112
Maíz Apellániz J., Pantaleoni González M., Barbá R. H., García-Lario P., Nogueras-Lara F., 2020, MNRAS, 496, 4951
Majewski S. R., Zasowski G., Nidever D. L., 2011, ApJ, 739, 25
Marigo P. et al., 2017, ApJ, 835, 77
Matsunaga N. et al., 2011, Nature, 477, 188
Matsunaga N. et al., 2016, MNRAS, 462, 414
Matsunaga N., Bono G., Chen X., de Grijs R., Inno L., Nishiyama S., 2018, Space Sci. Rev., 214, 74
McWilliam A., Zoccali M., 2010, ApJ, 724, 1491
Molnar T. A., Sanders J. L., Smith L. C., Belokurov V., Lucas P., Minniti D., 2022, MNRAS, 509, 2566
Morris M., Serabyn E., 1996, ARA&A, 34, 645
Nandakumar G. et al., 2018, A&A, 609, A109
Ness M. et al., 2013, MNRAS, 430, 836
Nishiyama S. et al., 2006, ApJ, 647, 1093
Nishiyama S., Nagata T., Tamura M., Kandori R., Hatano H., Sato S., Sugitani K., 2008, ApJ, 680, 1174
Nishiyama S., Tamura M., Hatano H., Kato D., Tanabé T., Sugitani K., Nagata T., 2009, ApJ, 696, 1407
Nishiyama S. et al., 2013, ApJ, 769, L28
Nogueras-Lara F. et al., 2018, A&A, 610, A83
Nogueras-Lara F., Schödel R., Najarro F., Gallego-Calvente A. T., Gallego-Cano E., Shahzamanian B., Neumayer N., 2019a, A&A, 630, L3
Nogueras-Lara F. et al., 2019b, A&A, 631, A20
Nogueras-Lara F. et al., 2020a, Nat. Astron., 4, 377
Nogueras-Lara F., Schödel R., Neumayer N., Gallego-Cano E., Shahzamanian B., Gallego-Calvente A. T., Najarro F., 2020b, A&A, 641, A141
Nogueras-Lara F., Schödel R., Neumayer N., 2021, A&A, 653, A133
Paczyński B., Stanek K. Z., 1998, ApJ, 494, L219
Pietrzyński G., Gieren W., 2002, AJ, 124, 2633
Price-Whelan A. M. et al., 2018, AJ, 156, 123
Ramírez S. V., Arendt R. G., Sellgren K., Stolovy S. R., Cotera A., Smith H. A., Yusef-Zadeh F., 2008, ApJS, 175, 147
Rattenbury N. J., Mao S., Sumi T., Smith M. C., 2007, MNRAS, 378, 1064
Rodrigo C., Solano E., 2020, in Contributions to the XIV.0 Scientific Meeting (virtual) of the Spanish Astronomical Society. p. 182
Rodrigo C., Solano E., Bayo A., 2012, SVO Filter Profile Service Version 1.0, IVOA Working Draft
Rojas-Arriagada A. et al., 2014, A&A, 569, A103
Rojas-Arriagada A. et al., 2020, MNRAS, 499, 1037
Ruiz-Dern L., Babusiaux C., Arenou F., Turon C., Lallement R., 2018, A&A, 609, A116
Saito R. K. et al., 2012, A&A, 537, A107
Sanders J. L., Smith L., Evans N. W., Lucas P., 2019, MNRAS, 487, 5188
Schlafly E. F., Finkbeiner D. P., 2011, ApJ, 737, 103
Schlafly E. F. et al., 2016, ApJ, 821, 78
Schlafly E. F. et al., 2018, ApJS, 234, 39
Schlafly E. F., Meisner A. M., Green G. M., 2019, ApJS, 240, 30
Schödel R., Najarro F., Muzic K., Eckart A., 2010, A&A, 511, A18
Schödel R., Feldmeier A., Neumayer N., Meyer L., Yelda S., 2014, Class. Quantum Gravity, 31, 244007
Schönrich R., Aumer M., Sale S. E., 2015, ApJ, 812, L21
Schultheis M. et al., 2014, A&A, 566, A120
Schultheis M., Rich R. M., Origlia L., Ryde N., Nandakumar G., Thorsbro B., Neumayer N., 2019, A&A, 627, A152
Simion I. T., Belokurov V., Irwin M., Koposov S. E., Gonzalez-Fernandez C., Robin A. C., Shen J., Li Z. Y., 2017, MNRAS, 471, 4323
Smith L. C. et al., 2018, MNRAS, 474, 1826
Sormani M. C., Binney J., Magorrian J., 2015, MNRAS, 454, 1818
Sormani M. C. et al., 2022, MNRAS, 512, 1857
Soto M. et al., 2019, MNRAS, 488, 2650
Stanek K. Z., Garnavich P. M., 1998, ApJ, 503, L131
Stanek K. Z., Mateo M., Udalski A., Szymanski M., Kaluzny J., Kubiak M., 1994, ApJ, 429, L73
Stanek K. Z., Udalski A., SzymaŃski M., KaŁuŻny J., Kubiak Z. M., Mateo M., KrzemiŃski W., 1997, ApJ, 477, 163
Stead J. J., Hoare M. G., 2009, MNRAS, 400, 731
Stelter R. D., Eikenberry S. S., 2021, ApJ, 911, 139
Surot F., Valenti E., Gonzalez O. A., Zoccali M., Sökmen E., Hidalgo S. L., Minniti D., 2020, A&A, 644, A140
Tang J., Bressan A., Rosenfield P., Slemer A., Marigo P., Girardi L., Bianchi L., 2014, MNRAS, 445, 4287
van der Walt S., Colbert S. C., Varoquaux G., 2011, Comput. Sci. Eng., 13, 22
Virtanen P. et al., 2020, Nat. Methods, 17, 261
Wang S., Chen X., 2019, ApJ, 877, 116
Wang S., Jiang B. W., 2014, ApJ, 788, L12
Waskom M. L.,2021, Journal of Open Source Software, 6, 3021
Wegg C., Gerhard O., 2013, MNRAS, 435, 1874
Wegg C., Gerhard O., Portail M., 2015, MNRAS, 450, 4050
Zasowski G. et al., 2009, ApJ, 707, 510
Zoccali M. et al., 2003, A&A, 399, 931
Zoccali M. et al., 2014, A&A, 562, A66
Zoccali M. et al., 2017, A&A, 599, A12

SUPPORTING INFORMATION

Supplementary data are available at *MNRAS* online.

Please note: Oxford University Press is not responsible for the content or functionality of any supporting materials supplied by the authors. Any queries (other than missing material) should be directed to the corresponding author for the article.

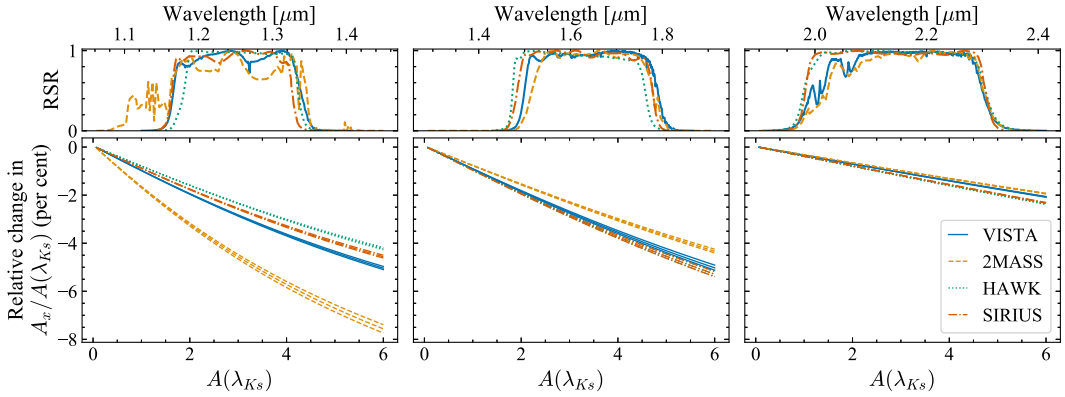

Figure A1. Comparison of the non-linearity of the extinction law in 2MASS (solid), VISTA (dashed), HAWK-I (dotted), and SIRIUS (dash-dot) J (left-hand panel), H (centre), and K_s (right-hand panel) bands. We display curves of the relative percentage change in the extinction in band x, A_x (evaluated using equation 1), normalized by the extinction evaluated at $\lambda_{K_s} = 2.149$ μm. For each band, three curves are shown corresponding to three giant spectra as described in Section 2.1 and we use the extinction curve from Fritz et al. (2011). The top row of panels shows the relative spectral response of each filter.

APPENDIX A: NON-LINEARITY OF *JHK*$_s$ EXTINCTION BANDS

As a complement to Fig. 1, we provide equivalent plots comparing the non-linearities in the 2MASS, VISTA, HAWK-I, and SIRIUS J, H, and K_s bands in Fig. A1. The strength of the non-linearities is related to the width of the photometric band: J_{2MASS} has significant non-linearities due to the blue transmission.

APPENDIX B: 2D EXTINCTION MAPS

Reliable extinction maps are an essential part of the interpretation of data for the central regions of our Galaxy. For simplicity, in this paper we work with 2D extinction maps and neglect the variation of the extinction along the line of sight. Whilst such an approach may be problematic when considering foreground or background stars, the 2D methods tend to measure the mean extinction to the highest stellar density regions. In this section, we use the extinction law derived in the main body of the paper to map the K_s extinction using two methods: (i) the red clump method and (ii) the Rayleigh Jeans colour excess method.

B1 Red clump method

A standard method for measuring the mean extinction for a region of the sky is to find the $(J-K_s)$ colour of the red clump and attribute the difference with respect to a standard value $(J-K_s)_0$ as due entirely to extinction (Gonzalez et al. 2011, 2012; Surot et al. 2020). For a population of stars with $(J-K_s) > 0.5$, within a colour–magnitude cut encompassing the red clump $11.5 < K_s - 0.482(J-K_s) < 14$ and with magnitude uncertainties < 0.2 mag, we find the colour of the red clump as the location of the maximum density from a multi-Gaussian fit (using the Bayesian information criterion to choose the number of components) and measure its width from the full-width at half-maximum. We avoid misidentifying the overdensity due to young turn-off stars by ensuring the peak is always located at < 20 per cent the colour range for $(J-K_s)$ at $|b| < 2$ deg. The choice of $(J-K_s)_0$ requires some care for precision work. Gonzalez et al. (2012) use $(J-K_s)_0 = 0.68$ based on measurements of extinction in other bands in Baade's window and using an assumed extinction law, whilst Simion et al. (2017) use $(J-K_s)_0 = 0.62$. We opt to 'zero-point' the $E(J-K_s)_{RC}$ measurements using the sample of RR Lyrae from Molnar et al. (2022). We select high-confidence RR Lyrae (classification probability >0.9) within $|\ell| < 1.5$ deg and $|b| < 1.5$ deg and with $E(J-K_s)_{RC} < 3$ to avoid biases at high extinction discussed below (assuming initially $(J-K_s)_0 = 0.62$ but this does not matter). We compute the sample's unextincted $(J-K_s)$ using the period–luminosity–metallicity relations from Cusano et al. (2021, also derived on the VISTA system) assuming [Fe/H]$= -0.94$ dex (Dékány, Grebel & Pojmański 2021, although the gradient of $(J-K_s)$ with metallicity is 0.007 mag dex^{-1} so varying the metallicity within reasonable values has a very weak effect). The peak distance of this sample is 8.22 kpc (assuming $(J-K_s)_0 = 0.62$ and $A_{Ks}/E(J-K_s) = 0.44$ as found in the main body of the paper) giving confidence that these RR Lyrae are behind a similar level of extinction to the red clump stars. We find $(J-K_s)_{RC} - E(J-K_s)_{RRL} \equiv (J-K_s)_0 = (0.647 \pm 0.004)$. This is redder than the solar neighbourhood $(J-K_s)_0 = (0.588 \pm 0.006)$ from Chan & Bovy (2020, transformed to the VISTA system using the equations from González-Fernández et al. 2018) due to the correlation between effective temperature and metallicity for red clump stars.

For regions of high extinction, the J photometry of red clump stars at the Galactic centre becomes incomplete and so extinction estimates via this method are biased low. In these regions $(H-K_s)$ is a better extinction estimator although in lower extinction regions it lacks the dynamic range of $(J-K_s)$. We employ the same procedure for $(H-K_s)$ with a selection $(H-K_s) > 0$ and $11.5 < K_s - 1.13(H-K_s) < 14$, avoiding the turn-off by ignoring peaks < 10 per cent for $(H-K_s)$ for $|b| < 1.5$ deg. We cannot zero-point the $(H-K_s)$ excesses using the RR Lyrae sample as no H-band period–luminosity relation is available from Cusano et al. (2021). We instead reference with respect to $E(J-K_s)_{RC}$ at low extinction assuming $E(J-K_s)/E(H-K_s) = 2.879$ from Table 1. Restricting to stars with $E(J-K_s)_{RC} < 3$ to avoid the underestimates at high extinction, we find $(H-K_s)_0 = (0.142 \pm 0.001)$. This agrees very well with the median $(H-K_s) = (0.130 \pm 0.001)$ of low extinction ($A_{Ks} < 0.01$) APOGEE DR17 (García Pérez et al. 2016; Abdurro'uf et al. 2022) stars with $2.3 < \log g < 2.5$ and $0.63 < (J-K_s) < 0.67$ using the transformations from 2MASS to VISTA from González-Fernández et al. (2018).

Another consideration is resolution: extinction often varies on very small scales but we must average over sufficiently large patches of sky to yield enough red clump stars. However, because of extinction, the number density of stars varies on small scales making a fixed resolution inappropriate. Wegg & Gerhard (2013) use the Gonzalez et al. (2011) method employing an adaptive resolution. Here we follow a similar procedure using the properties of the nested HEALPIX

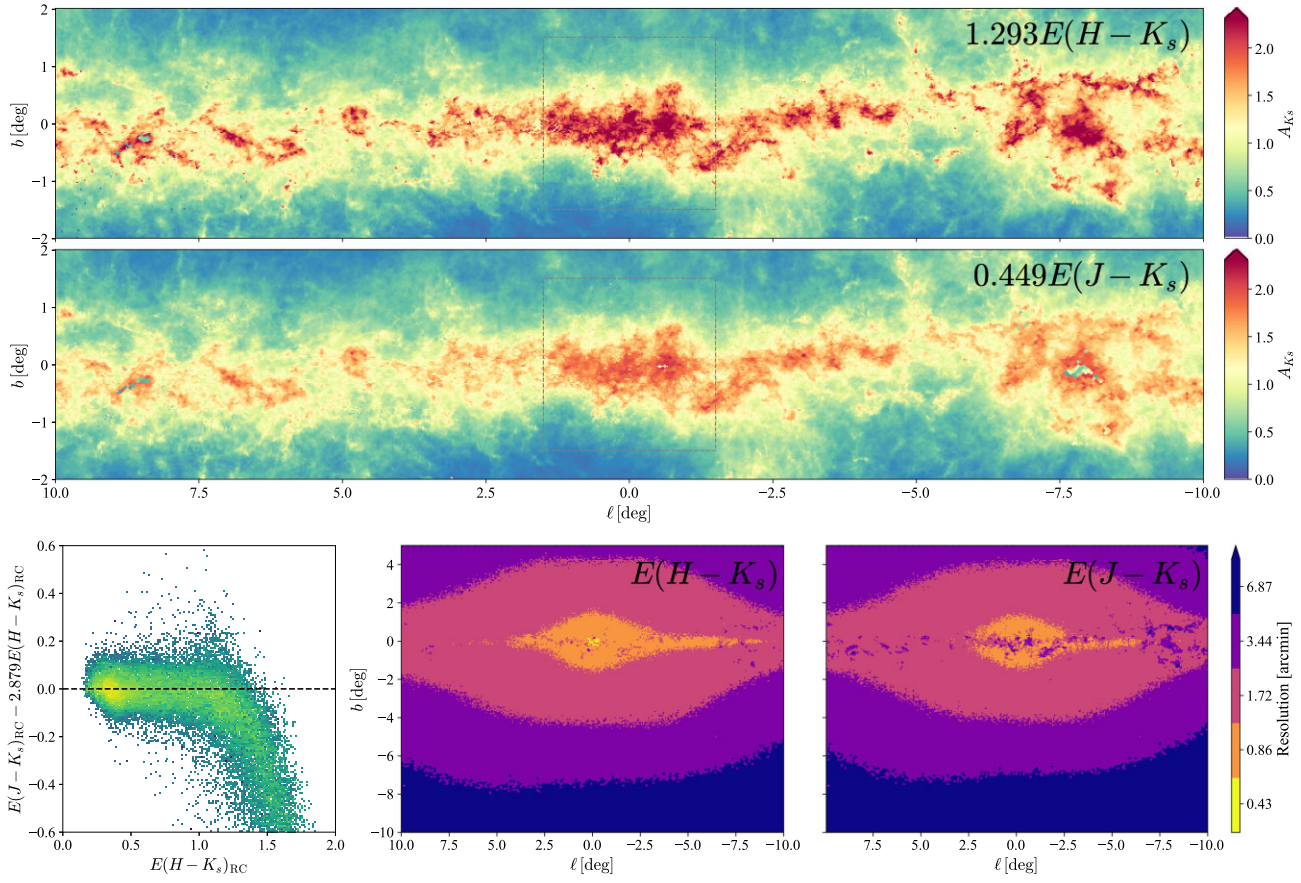

Figure B1. Adaptive resolution extinction maps. The top two panels show the A_{K_s} extinction computed from the $(H-K_s)$ and $(J-K_s)$ colours of the red clump stars (the grey box gives the region studied in this paper). The bottom left-hand panel shows the difference between the map pixels assuming $E(J-K_s)/E(H-K_s) = 2.879$ as per Table 1. The high extinction regions have underestimated $E(J-K_s)$ as the Galactic centre/bulge red clump stars are lost in VIRAC2 J in these regions. The right two panels in the bottom row shows the adaptively chosen resolution of the maps such that >100 red clump stars are in each pixel.

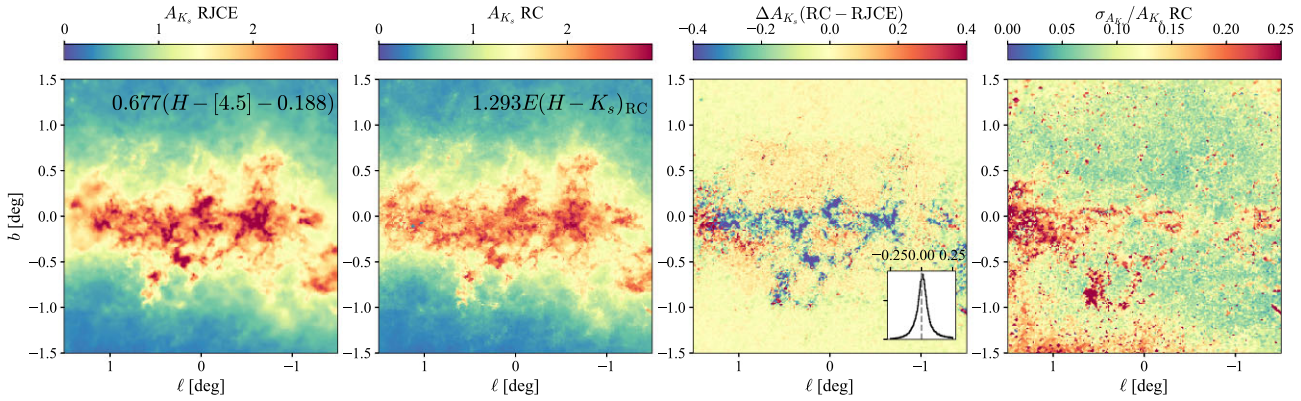

Figure B2. Comparison of extinction maps computed using the RJCE method (first panel) and the red clump method (second panel). The difference is shown in the third panel. Note the good correspondence except within the very high extinction regions where the bulge red clump is not visible in VIRAC2 H so extinction is underestimated by the red clump method. Note also the general overestimate in the central $-1 \lesssim \ell \lesssim 1$ and $-0.7 \lesssim b \lesssim 0.7$ potentially due to zero-point differences between the two *Spitzer* surveys, Ramírez et al. (2008) and Churchwell et al. (2009). The right-hand panel shows the relative uncertainty in the red clump extinction estimates.

scheme (Fernique et al. 2014). We first bin stars using a HEALPIX NSIDE of 256 (angular resolution of 13.7 arcmin) and subdivide each bin individually until any more subdivision would produce fewer than 100 stars per bin. This produces resolutions down to 0.3 arcmin. The advantage of using the nested HEALPIX scheme is that each index can be simply converted to an index at the highest resolution of the map. A query for the extinction at a given location is then a fast binary search for where the index of the required HEALPIX sits within the list of sorted pixels. The extinction is that of the entry below the insertion point. The resolution of our maps is inferior to the recent

work from Surot et al. (2020) who use a similar method but require only 20 stars to produce an extinction estimate. The resulting maps are consistent with ours but have a larger scatter from using fewer stars.

In Fig. B1, we display the K_s extinction maps within the bulge mid-plane $|b| < 2$ deg derived from the red clump $(H - K_s)$ and $(J - K_s)$ colours along with the resolution maps across the entire bulge. The extinction coefficients are taken from Table 3. We observe excellent correlation between the two maps in lower extinction regions. It is clear the $(J - K_s)$ map underestimates the extinction in regions of high extinction due to the red clump stars being too faint in J in these fields. In many cases, foreground red giants with lower extinction are identified causing slight underestimates, but in extreme cases (e.g. $(\ell, b) = (-8, 0)$ deg) the algorithm has possibly identified young main sequence stars as red clump stars leading to severe underestimates. The resolution maps largely trace the stellar density (note the bar-bulge asymmetry). In low-latitude, high-extinction regions, the J resolution is decreased.

B2 Rayleigh Jeans colour excess method

As with the J photometry, H of the bulge red clump becomes incomplete in some high extinction regions, producing biased results. In these regions we can employ an alternative method that uses all red giant stars so is less reliant on observing the red clump. Majewski et al. (2011) introduced the 'Rayleigh Jeans Colour Excess' method by showing how red giants have a near constant intrinsic $(H - [4.5])$ colour such that the extinction can be estimated as $A_{Ks} = 0.918(H - [4.5] - 0.08)$ based on the extinction law from Indebetouw et al. (2005). Soto et al. (2019) used this technique with VVV and GLIMPSE data in the southern disc. Recently, Stelter & Eikenberry (2021) have used the RJCE method on integrated photometry of the Galactic centre region finding an infrared slope of $\alpha = (2.03 \pm 0.06)$. We use the sample of VIRAC2 sources cross-matched to the GLIMPSE catalogue (Churchwell et al. 2009) and the *Spitzer*-IRAC GALCEN point source catalogue of Ramírez et al. (2008) using a 0.4 arcsec cross-match radius, as detailed in Section 2.2. This uses stars with [4.5] magnitude uncertainties <0.2, H uncertainties <0.06, no neighbour within 1 arcsec, no potential AGB or YSO stars (using $([5.8] - [8.0])$) and the cuts on extinction-corrected $(H - K_s)$ and $(J - K_s)$ (when available) to remove potential foreground contaminants. We have calibrated the relationship between $E(H - K_s)$ and $(H - [4.5])$ using the method in Section 2. We fix $E(H - [4.5])/E(H - K_s)$ using the coefficient from Table 1 and fit for the intercept of $(H - [4.5])$ versus $E(H - K_s)_{\rm RC}$ accounting for non-linearities and the giant branch slope. We find $E(H - [4.5]) = 0.967(H - [4.5] + 0.0482(K_s - 12.514) - 0.210)$. Note the non-unity leading coefficient is due to the slight gradient of the giant branch in $(H - [4.5])$. Combining with the $A_{Ks}/E(H - [4.5])$ found in the main body of the paper we find

$$A_{Ks} = 0.677(H - [4.5] - 0.188), \quad \text{(B1)}$$

for $K_s = 13$ stars. The zero-point of $(H - [4.5])_0 = 0.19$ is redder than that used by Majewski et al. (2011) based on the Girardi et al. (2002) isochrones. This could be linked to zeropoint issues in the photometry or population effects, particularly as the red clump stars in this region also appear intrinsically redder in $(J - K_s)$ and $(H - K_s)$ than in the solar neighbourhood. For a set of Healpix with NSIDE of 8192 (26 arcsec resolution), we find the 100 nearest neighbours to the centre of the pixel and measure the median $E(H - [4.5])$ colour and its spread.

In Fig. B2 we display a comparison of the maps derived using the RJCE method with those from the red clump method. We see from the difference map that on the average the maps match well, but in the high extinction regions of the mid-plane the red clump method significantly underestimates the extinction. For the high extinction regions the red clump stars in the centre of the Galaxy are too faint in H for VIRAC2 so the average $E(H - K_s)_{\rm RC}$ extinction measurement is to foreground red clump stars. There is a general discrepancy (faint red/orange) in the central $-1 \lesssim \ell \lesssim 1$ and $-0.7 \lesssim b \lesssim 0.7$ corresponding to the footprint of the Ramírez et al. (2008) survey with the RJCE method underestimating the extinction relative to the RC method. Ramírez et al. (2008) report their [4.5] measurements being 0.06 mag fainter in the mean than the GLIMPSE measurements in the overlapping regions consistent with this bias. We also note the region around $(\ell, b) = (1.25, 0)^\circ$ where the RJCE method underestimates the extinction. It appears that here there is a significant contribution from young stars. This suggests there is important variation of the extinction along the line of sight for this region and highlights the limitations of our method. We can see that clearly in the map of the relative spread in extinction from $(H - K_s)$ red clump method (the spread from the RJCE method displays a similar feature) where this region is one of the most significant, along with the feature at $(\ell, b) = (0.5, -0.8)^\circ$.

APPENDIX C: COMPLETENESS OF THE VIRAC2 CATALOGUE

In this work we have measured the density profile of red clump stars. For this, we require knowledge of the incompleteness of the source catalogue i.e. the probability of a source with a given magnitude and on-sky location being detected under given observing conditions. Incompleteness arises from seeing and sky brightness limitations which alter the limiting magnitude depth of a survey and can result in blending in crowded regions. Traditionally, incompleteness has been assessed through two methods. In some cases, a deeper, more complete catalogue is available to which we can exactly compare which sources in our catalogue of interest were detected. However, for the VVV survey, no such deeper catalogue is available across the entirety of the survey footprint and so we must instead estimate the source recovery rate another way. One method for assessing this is through testing the recovery of artificial stars injected into the reduction pipeline. VIRAC v1 used aperture photometry for which Saito et al. (2012) performed these artificial star tests. Here we will follow this method by checking the recovery of artificial stars using point-spread-function photometry utilized in VIRAC2 and we will use the method of comparison to deeper catalogues as a cross-check in survey regions overlapping deeper surveys.

In a stacked image (a combination of two dithered images) from a single detector, we inject artificial stars arranged on a regular hexagonal grid spaced by 30 pixels (typical seeing is ∼2.2 pixels). This results in ∼5700 stars being injected. The stars are assigned magnitudes randomly sampled between $K_s = 10$ mag and $K_s = 20$ mag, and follow a Gaussian point-spread-function with full-width at half-maximum equal to the seeing stored in the header for each image. The fake image is processed using DoPhot using the same configuration parameters as adopted by Smith et al. (in preparation). An artificial star is 'recovered' if there is an output source approximately within 1 pixel (0.339 arcsec assessed using a k-d tree) and 1 mag of the input, and the source also lies within a region of the associated CASU confidence map (Emerson et al. 2004) with value >25. We store the fraction of sources recovered in bins of 0.2 mag and apply a Gaussian smoothing filter of one bin width.

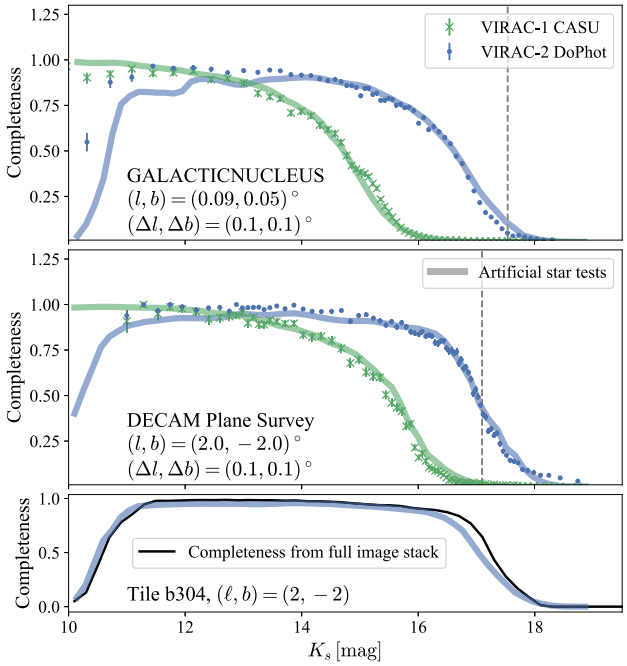

Figure C1. VIRAC completeness tests: the top two panels show the completeness for two 0.1 deg by 0.1 deg fields centred on $(\ell, b) = (0.19, 0.18)$ deg (top) and $(\ell, b) = (4, 2)$ deg (bottom). Solid lines show the expected completeness from artificial star tests and the points with errorbars (blue dots for VIRAC2 which uses DoPhot and green crosses for VIRAC v1 which uses CASU's aperture photometry program *imcore*) show the completeness measured with respect to the GALACTICNUCLEUS (top) and DECAPS catalogues (bottom). The dashed lines show the magnitudes at which the magnitude distributions of GALACTICNUCLEUS and DECAPS turn over. The bottom panel shows a check of our simple completeness procedure using a representative set of images (thick blue) compared to the results of analysing a full image stack (thin black).

This procedure is repeated for all 16 detectors, although we ignore the results from detector 4 which is known to have a number of bad rows (see the CASU webpages). Note that our procedure ignores completeness variations within a single detector image, which could arise due to variations in the detector properties or variations in crowding. This is a particularly noticeable issue near the nuclear star cluster where there is large density variation on a sub-detector level. Under the assumption of uniform density, our completeness estimates will, in general, underestimate the completeness correction slightly as more stars lie in higher crowding regions which have lower completeness. In this way, the star-weighted completeness over a detector image is lower than that estimated from our uniform distribution of artificial stars.

The VIRAC2 catalogue is a multi-epoch astrometric catalogue so the probability of a source entering the catalogue depends on the probability of detection in every image. Typically DoPhot reports a number of false detections, which can arise, for instance, in the wings of bright sources. Therefore, reliable sources require detection in multiple images, or other quality cuts. However, performing the artificial star tests on every image is a costly procedure, and many images will have very similar completeness properties. We therefore opt to only perform the artificial star tests on representative sets of images. Two typical quality cuts employed on the VIRAC2 data set are requiring a five-parameter astrometric solution (at least 10 epochs – typically fields have > 100 epochs) and/or that the source is detected in more than 20 per cent of the observations. For each unique bulge

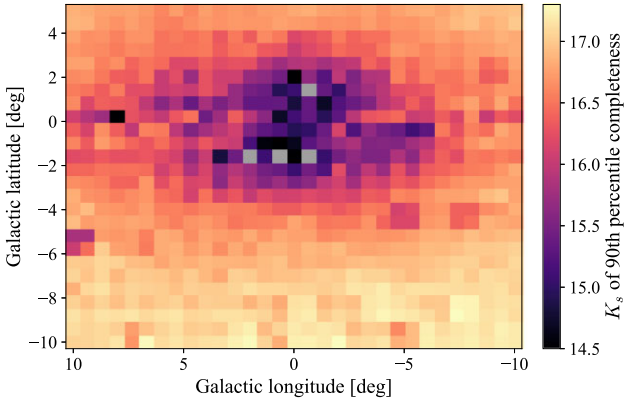

Figure C2. K_s magnitude at which the bulge region of VIRAC2 is 90 per cent complete. The grey pixels are regions where 90 per cent completeness is not reached for any magnitude.

tile and pointing combination (6 pointings per tile), we perform our procedure on the images at the 2nd, 20th, and 80th percentiles of seeing. We choose the 2nd as this represents the 'best' completeness, 20th as it corresponds to at least 20 per cent detection rate at the faint end and 80th to correspond to at least 20 per cent detection rate at the faint end. Each set includes $196 \times 6 \times 16 = 18,816$ individual detector images so we process a total of ∼55 000 images. We combine the results of the 20th and 80th percentile results taking the maximum completeness at each K_s, and use these values as our standard completeness values.

The resulting catalogue of completeness ratios as a function of (ℓ, b, K_s) is interpolated on to a regular grid using inverse distance weighting of 5 nearest neighbours. This regular grid is then interpolated using cubic splines for any required point. We perform a cross-check of our procedure by adding a set of artificial stars into all images in a single tile: b304 centred around $(\ell, b) \approx (-2, -2)$ deg. We first create a hexagonal grid of sources in equatorial coordinates spaced by 30 VIRCAM pixels (10.2 arcsec) over the area covered by the tile (approximately 260 000 stars) and assign random magnitudes as before. For each detector image we insert the stars at the appropriate pixel locations, process with DoPhot and check recovery as before. We record the total number of observations and detections for each artificial source. In the lower panel of Fig. C1 we show the ratio of the number of artificial sources with more than 20 per cent detections to the total number and compare to the expected completeness from the previous approach. We note the satisfactory agreement. From $K_s \approx 12$, our previous approach slightly underestimates the true completeness and this is most noticeable at the faint end. It appears this is due to the incorrect assumption that the completeness in the regions covered by overlapping images with similar seeing are equal in the two images. Particularly for fainter magnitudes, a similar fraction of sources is recovered in each image, but in the overlapping sections it is a slightly different set of sources. This means more sources in total are detected, slightly increasing the completeness fraction. Possibly this is related to varying performance across each detector. At the bright end, the well-matched turnover validates our procedure for combining the results of the 20th and 80th percentiles.

In Fig. C2 we show the on-sky distribution of the K_s magnitude at which the bulge region of VIRAC2 is 90 per cent complete. We see at high latitude the completeness is above 90 per cent down to magnitudes fainter than $K_s = 17$. For higher density regions near the mid-plane and inner bulge (the subject of this paper) the completeness is above 90 per cent only below $K_s \approx 15.5$.

C1 Comparison with external catalogues

We validate our procedure by inspecting the expected completeness ratio against that measured by comparison to the GALACTICNUCLEUS survey (Nogueras-Lara et al. 2019b) and the DECAM Plane Survey (Schlafly et al. 2018). The GALACTICNUCLEUS survey is a JHK_s imaging survey using HAWK-I on the VLT reaching a 5σ depth of $K_s \approx 21$. The survey has 49 pointings of 7.5 arcmin by 7.5 arcmin primarily located within the nuclear stellar disc, but several pointings lie slightly out of the mid-plane. Nogueras-Lara et al. (2019b) estimates the catalogues are ~ 80 per cent complete at $K_s = 16$ mag. The difference between K_s measurements for VIRAC2 versus GALACTICNUCLEUS is 0.06 mag for the field inspected below. DECAM Plane Survey (DECAPS) is a *grizY* imaging survey using the Dark Energy Camera at Cerro Tololo covering $-120 < \ell/\,\mathrm{deg} < 5$ and $|b| \lesssim 4$ deg. The survey has a 6σ depth in Y of 21. We compute an approximate K_s magnitude from *izY* using $K_s \approx i - 3.34(i - z) - 1.98(z - y) - 0.69$ (this only works well for low extinction regions – the region we choose has $A_{K_s} \approx 0.2$ mag).

Fig. C1 shows the completeness of two fields with respect to the GALACTICNUCLEUS and DECAPS catalogues alongside the expectation from the artificial star tests. We display the ratio of sources that have a cross-match in VIRAC2 as a function of K_s (using the approximate K_s for DECAPS). The two fields are 0.1 deg by 0.1 deg centred on $(\ell, b) = (0.19, 0.18)$ deg and $(\ell, b) = (4, 2)$ deg. In these fields, there are respectively ∼670 000 and ∼2.3 million sources per square deg with $K_s < 16$ in VIRAC2. We note the very good correspondence between expected and measured completeness. We naturally expect small differences as the parent catalogues (GALACTICNUCLEUS and DECAPS) are not perfectly complete. Indeed 2 and 5 per cent of sources in the VVV catalogue are not cross-matched within 0.4 arcsec to any source in the GALACTICNUCLEUS and DECAPS catalogue respectively. Additionally, we show the magnitudes at which the magnitude distributions of GALACTICNUCLEUS and DECAPS begin turning over (∼17.5 and ∼17, respectively). This magnitude is a good indicator of the point at which a catalogue starts becoming incomplete. For both comparison fields, our completeness calculations match the recovery ratio very well. We also display the equivalent results for the VIRAC v1 catalogue which used the CASU aperture photometry software *imcore*. In the DECAPS field there is ∼1 magnitude increase in the 50 per cent completeness level of VIRAC2 compared to v1 which increases to ∼2 magnitudes for the highly crowded GALACTICNUCLEUS field.

This paper has been typeset from a TEX/LATEX file prepared by the author.